

1 Visibility-derived aerosol optical depth over global land from 1980 to 2 2021

3 Hongfei Hao¹, Kaicun Wang², Chuanfeng Zhao³, Guocan Wu¹, Jing Li³

4 ¹Global Change and Earth System Science, Faculty of Geographical Science, Beijing Normal
5 University, Beijing 100875, China

6 ²Institute of Carbon Neutrality, Sino French Institute of Earth System Science, College Urban and
7 Environmental Sciences, Peking University, Beijing 100871, China

8 ³Institute of Carbon Neutrality, Department of Atmospheric and Oceanic Sciences, School of
9 Physics, College Urban and Environmental Sciences, Peking University, Beijing 100871, China

10 *Corresponding Author: Kaicun Wang (kcwang@pku.edu.cn)*

11 Abstract

12 Long-term and high spatial resolution aerosol optical depth (AOD) data are essential for climate
13 change detection and attribution. Global ground-based AOD observations ~~stations~~ are sparsely
14 distributed, and satellite AOD ~~retrievals observations~~ have a low temporal frequency, as well low
15 accuracy before 2000 over land. In this study, AOD is derived from hourly visibility observations
16 collected at more than 5000 meteorological stations over global land from 1980 to 2021. The AOD
17 retrievals of the Moderate Resolution Imaging Spectroradiometer (MODIS) onboard the Aqua Earth
18 observation satellite are used to train the machine learning model, and the ERA5 reanalysis
19 boundary layer height is used to convert the surface visibility to AOD. Comparisons with
20 independent datasets show that the predicted AOD has correlation coefficients of ~~0.54 and~~ 0.55 with
21 ~~Terra MODIS satellite retrievals and~~ AERONET ground observations at daily time scale. The
22 correlation coefficients are higher at monthly and annual scales, which are ~~0.81 and~~ 0.61 for the
23 monthly and ~~0.91 and~~ 0.65 for the annual, ~~compared with Terra MODIS and AERONET AOD,~~
24 respectively. The visibility-derived AOD at station scale is gridded into a 0.5° grid by ordinary
25 kriging interpolation. The mean visibility-derived AOD over the global land (-60°N-85°N), the
26 Northern Hemisphere, and the Southern Hemisphere are 0.161, 0.158, and 0.173, with a trend of -
27 0.0026/10a, -0.0018/10a, and -0.0059/10a from 1980 to 2021. For the regional scale, the mean (trend)
28 of AOD are 0.145 (-0.0041/10a), 0.139 (-0.0021/10a), 0.131 (-0.0009/10a), 0.153 (-0.0021/10a),
29 0.192 (-0.0100/10a), 0.275 (-0.0008/10a), 0.177 (-0.0096/10a), 0.127 (-0.0081/10a), 0.177 (-
30 0.0003/10a), 0.222 (-0.0000/10a), 0.232 (0.0071/10a), and 0.255 (0.0096/10a) in Eastern Europe,
31 Western Europe, Western North America, Eastern North America, Central South America, Western
32 Africa, Southern Africa, Australia, Southeast Asia, Northeast Asia, Eastern China, and India. The
33 visibility-derived AOD at station and grid scales over global land from 1980 to 2021 are available
34 at National Tibetan Plateau / Third Pole Environment Data Center
35 (<https://doi.org/10.11888/Atmos.tpdc.300822>) (Hao et al., 2023).

36 How to cite. Hao, H., Wang, K., C. Zhao, Wu, G., J. Li (2023). Visibility-derived aerosol optical
37 depth over global land (1980-2021). National Tibetan Plateau / Third Pole Environment Data

39 **1 Introduction**

40 Atmospheric aerosols are composed of solid and liquid particles suspended in the atmosphere.
41 Aerosol particles are directly emitted into the atmosphere or formed through gas-particle
42 transformation (Calvo et al., 2013), with diverse shapes and sizes (Fan et al., 2021), optical
43 properties, and ~~various~~-components (Liao et al., 2015; Zhang et al., 2020; Li et al., 2022). Most
44 atmospheric aerosols are concentrated in the troposphere, especially in the boundary layer (Liu et
45 al., 2022), with a high concentration near emission sources (Kulmala et al., 2004) , and a small
46 portion are distributed in the stratosphere. Atmospheric aerosols severely impact the atmospheric
47 environment and human health. They deteriorate air quality, reduce visibility, and cause other
48 environmental issues (Wang et al., 2012; Boers et al., 2015). They impair human health or other
49 organisms' conditions by increasing cardiovascular and respiratory disease incidence and mortality
50 rates (Chafe et al., 2014; Yang et al., 2022). The Global Burden of Disease shows that global
51 exposure to ambient PM_{2.5} (particulate matter suspended in air with an aerodynamic diameter of
52 less than 2.5 micrometers) resulted in 0.37 million deaths and 9.9 million disability-adjusted life
53 years (Chafe et al., 2014).

54 Aerosols are inextricably linked to climate change. Atmospheric aerosols alter the Earth's energy
55 budget and then affect the climate (Li et al., 2022). They cool the surface and heat the atmosphere
56 by scattering and absorbing solar radiation (Forster et al., 2007; Chen et al., 2022). Aerosols, such
57 as black carbon and brown carbon, also absorb solar radiation (Bergstrom et al., 2007), heat the
58 local atmosphere and suppress or invigorate convective activities (Ramanathan et al., 2001; Sun and
59 Zhao, 2020). Aerosols also alter the optical properties and life span of clouds (Albrecht, 1989).
60 Atmospheric aerosols strongly affect regional and global short-term and long-term climates through
61 direct and indirect effects (McNeill, 2017).

62 Tropospheric aerosols are considered as the second largest forcing factor for global climate change
63 (Li et al., 2022), and they reduce the warming due to greenhouse gases by -0.5°C (Ipcc, 2021).
64 However, aerosols are also regarded as the largest contributor to quantifying the uncertainty of
65 present-day climate change (Ipcc, 2021). The uncertainties are caused by the deficiencies of the
66 global descriptions of aerosol optical properties (such as scattering and absorption) and
67 microphysical properties (such as size and component), and the impact on cloud and precipitation,
68 further affecting the estimation of aerosol radiative forcing (Lee et al., 2016; Ipcc, 2021). Therefore,
69 sufficient aerosol observations are crucial. In aerosol measurements, aerosol optical depth (AOD)
70 is often used to describe its column properties, which represents the vertical integration of aerosol
71 extinction coefficients. AOD is an important physical quantity for estimating the content,
72 atmospheric pollution and climatology of aerosols (Zhang et al., 2020).

73 AOD data usually from ground-based and satellite-borne remote sensing observations. They have
74 both advantages and disadvantages. Ground-based lidar observation is an active remote sensing
75 technology. Lidar generally emits laser and receives backscattered signals to invert the extinction
76 coefficient of aerosols at different heights (Klett, 1985). By using the depolarization ratio, the type
77 of aerosol, such as fine particles or dust, can be distinguished (Bescond et al., 2013). The AOD
78 within a certain height can be calculated by integrating the extinction coefficients; however,

79 scattering signals are usually not received near the ground, leading to blind spots (Singh et al., 2019).
80 At present, there are many ground-based lidar worldwide and regional networks, which provides
81 important support of vertical changes in aerosols, such as the NASA Micro-Pulse Lidar Network
82 (MPLNET) in the early 1990s (Welton et al., 2002), the European Aerosol Research Lidar Network
83 (EARLINET) since 2000 (Bösenberg and Matthias, 2003), the Latin American Lidar Network
84 (LALINET) since 2013 (Guerrero-Rascado et al., 2016).

85 Ground-based remote sensing observations supply aerosol loading data (such as AOD), by
86 measuring the attenuation of radiation from the top of the atmosphere to the surface (Holben et al.,
87 1998). This type of observations mainly uses weather-resistant automatic sun and sky scanning
88 spectral radiometers to retrieve optical and microphysical aerosol properties (Che et al., 2014). The
89 Aerosol Robotic Network (AERONET) is a popular global network composed of NASA and
90 multiple international partners that provides high-quality and high-frequency aerosol optical and
91 microphysical properties under various geographical and environmental conditions (Holben et al.,
92 1998; Dubovik et al., 2000). The AERONET observations are extensively used to validate satellite
93 remote sensing observations and model simulations, as well as climatology study (Dubovik et al.,
94 2002b). There are many regional networks of sun photometers, such as the Maritime Aerosol
95 Network (MAN), which use a handheld sun photometer to collect data over the ocean and is merged
96 into AERONET (Smirnov et al., 2009), the China Aerosol Robot Sun Photometer Network
97 (CARSNET) (Che et al., 2009), the Canadian sub-network of AERONET (AEROCAN) (Bokoye et
98 al., 2001), Aerosol characterization via Sun photometry: Australian Network (AeroSpan)
99 (Mukkavilli et al., 2019), and the sky radiometer network (SKYNET) in Asia and Europe (Kim et
100 al., 2004; Nakajima et al., 2020). Another very valuable global network is the NOAA/ESRL
101 Federated Aerosol Network (FAN), which uses integrated nephelometers distinct from sun
102 photometers, mainly located in remote areas, providing background aerosol properties over 30 sites
103 (Andrews et al., 2019).

104 Satellite remote-sensing is a space-based method that can provide aerosol properties worldwide.
105 With the development of satellite remote sensing technology since 1970s, aerosol distributions can
106 be extracted with the advantage of sufficient real-time and global coverage from multiple satellite
107 sensors (Kaufman and Boucher, 2002; Anderson et al., 2005). The Advanced Very High Resolution
108 Radiometer (AVHRR) is the earliest sensor used for retrieving AOD over ocean (Nagaraja Rao et
109 al., 1989). The Moderate Resolution Imaging Spectroradiometer (MODIS), on board the Terra
110 (launched in 1999) and Aqua (launched in 2002) satellites is a popular sensor with 36 channels,
111 which have been used for AOD retrieval over both ocean and land based on the Dark Target and the
112 Deep Blue algorithms (Remer et al., 2005; Levy et al., 2013). The latest MODIS AOD data version
113 is the Collection 6.1, which provides global AOD over 20 years (Wei et al., 2019). There are also
114 many other satellite sensors that can be used to retrieve AOD, such as the Polarization and
115 Directionality of the Earth's Reflectances (POLDER) during 1996-1997, 2003 and 2004-2013
116 (Deuzé et al., 2000), Sea-viewing Wide Field-of-view Sensor (SeaWiFS) during 1997-2007
117 (O'reilly et al., 1998), the Multi-angle Imaging Spectroradiometer (MISR) on Terra since 1999
118 (Diner et al., 1998). The Cloud-Aerosol Lidar with Orthogonal Polarization (CALIOP) has also
119 derived aerosols in the vertical direction since 2006 (Winker et al., 2009).

120 These measurements provide important data for studying the global and regional spatiotemporal
121 variabilities and climate effect of aerosols. However, ground-based remote sensing observations

122 only provide aerosol properties with low spatial coverage. There were only ~~1126~~ about 150 ground
123 stations worldwide in 2002 and even fewer sites were available for climate analysis (Holben et al.,
124 1998; Chu et al., 2002), which limited aerosol climate research by spatial coverage (Bright and
125 Gueymard, 2019). Satellite remote sensing overcomes the limitations of spatial coverage. The
126 AVHRR has been used to retrieve AOD since 1980, but it is limited by a few channel number, low
127 spatial resolution, and insufficient validation through ground-based observations before 2000 (Hsu
128 et al., 2017). Many studies have only investigated the trends and distributions of aerosols after 2000
129 (Bösenberg and Matthias, 2003; Winker et al., 2013; Xia et al., 2016; Tian et al., 2023), because of
130 the lack of long-term and global cover AOD products, which is the bottleneck for aerosol climate
131 change detection and attributions.

132 To overcome these limitations and enrich aerosol data, alternative observation data could be utilized
133 to derive AOD. Atmospheric horizontal visibility is a suitable alternative (Wang et al., 2009; Zhang
134 et al., 2020), because it has the advantages of the long-term records with a large number of stations
135 worldwide.

136 Atmospheric visibility is a physical quantity that describes the transparency of the atmosphere
137 through manual and automatic observations, and the automatic observations of visibility usually
138 measure atmospheric extinction (scattering coefficient and transmissivity). Koschmieder (1924)
139 first proposed the relationship between the meteorological optical range and the total optical depth.
140 Elterman (1970) further established a formula between AOD and visibility by assuming an
141 exponential decrease in aerosol concentration with altitude, considering the extinction of molecules
142 and ozone to analyze air pollution, which called the Elterman model. Qiu and Lin (2001) corrected
143 the Elterman model by considering the influence of water vapor and used two water vapor pressure
144 correction coefficients to retrieve AOD of 16 stations in China in 1990. Wang et al. (2009) analyzed
145 the trend of AOD using visibility-based retrievals from 1973 to 2007 over land. Lin et al. (2014)
146 retrieved the AOD in eastern China in 2006 using visibility and aerosol vertical profiles provided
147 by GEOS-Chem. Wu et al. (2014) and Zhang et al. (2017) parameterized the constants in the
148 Elterman model and use satellite retrieved AOD to solve the parameters in the models at different
149 stations, to retrieve the long-term AOD in China.

150 Zhang et al. (2020) reviewed the methods of visibility retrieval of AOD, indicating that visibility-
151 based retrieval of AOD can compensate for the shortcomings of long-term aerosol observation data.
152 Simultaneously, various parameters, such as station altitude, consistency of visibility data, water
153 vapor and aerosol vertical profiles (scale height), were discussed with modified suggestions
154 proposed. These studies have enriched AOD data regionally. These studies have enriched aerosol
155 data in some extent. At present, there are very few studies on global visibility-retrieved AOD and to
156 analyze climatology of aerosols.

157 The two physical quantities of visibility and AOD have both connections and differences, making it
158 challenging to retrieve AOD from visibility. Visibility represents the maximum horizontal visible
159 distance near the surface, while AOD represents the total vertical attenuation of solar radiation by
160 aerosols. The visibility of automatic observation is dependent on the local horizontal atmospheric
161 extinction (Noaa et al., 1998). Visibility has not a simple linear relationship with meteorological
162 factors. The vertical structure of aerosols is the greatest challenge to obtain, as it is not a simple
163 hypothetical curve in complex terrain and circulation conditions (Zhang et al., 2020). These

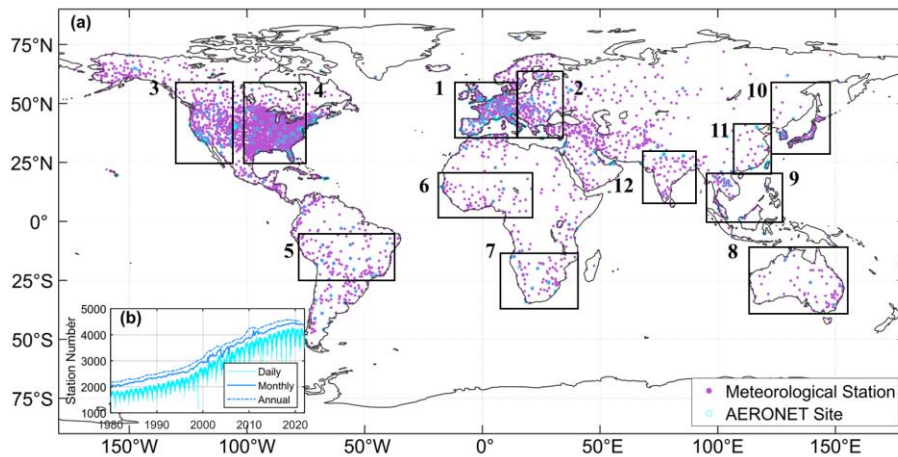
164 limitations make it more complex to derive AOD. Machine learning methods can effectively address
165 complex nonlinear relationships between variables and have been widely applied in remote sensing
166 and climate research fields. Li et al. (2021) used the random forest method to predict PM_{2.5} in Iraq
167 and Kuwait based on satellite AOD during 2001-2018. Kang et al. (2022) applied LightGBM and
168 random forest to estimate AOD over East Asia, and the results showed a consistency with
169 AERONET. Dong et al. (2023) derived aerosol single scattering albedo from visibility and satellite
170 AOD over 1000 global stations. Hu et al. (2019) used a deep learning method to retrieve horizontal
171 visibility from MODIS AOD. These studies have confirmed the ability of machine learning to
172 effectively solve complex relationships among variables. And previous studies are mostly
173 conducted at the regional or national scale, and few studies at the global scale. Thus, it is feasible to
174 derive AOD from atmospheric visibility over global land by using the machine learning method.

175 In this study, we propose a machine learning method to derive AOD, where satellite AOD is the
176 target value, and visibility and other related meteorological variables are the predictors. We explain
177 the robustness of the model, validate the model's predictions using independent ground-based AOD,
178 ~~and independent~~ satellite retrievals and reanalysis AOD, and analyze the mean and trend of AOD
179 across land and regions. Two datasets of long-term high-resolution AOD are generated. The Section
180 2 introduces the data and method. The Section 3 is the evaluation and validation of the visibility-
181 derived AOD, and the distribution and trends are discussed at global and regional scales. The Section
182 54 presents the conclusions. This study is dedicated to supporting the research of aerosols in climate
183 change detection and attribution.

184 **2 Data and method**

185 **2.1 Study area**

186 The study area is global land. A total of 5032 meteorological stations and 395 AERONET sites are
187 selected in this study, shown in Figure 1. Twelve regions are selected for special analysis, including
188 Eastern Europe, Western Europe, Western North America, Eastern North America, Central South
189 America, Western Africa, Southern Africa, Australia, Southeast Asia, Northeast Asia, Eastern China,
190 and India. The time range of the study is from 1980 to 2021, during which the records of
191 meteorological stations are sufficient with a uniform spatial distribution. As shown in Figure 1, the
192 daily records have exceeded 1500 stations, and monthly and annual records have exceeded 2000
193 during 1980-1990. After 2000, monthly records have reached 3000, which is the foundation of
194 gridding AOD.



195

196 **Figure 1:** Study area (a) and the meteorological station number (b) with daily, monthly, and annual
 197 records. The number of meteorological stations (filled circles) is 5032. The number of AERONET
 198 sites (empty circles) is 395. The box regions of labelled with number 1-12 are Eastern Europe,
 199 Western Europe, Western North America, Eastern North America, Central South America, Western
 200 Africa, Southern Africa, Australia, Southeast Asia, Northeast Asia, Eastern China, and India.

201 **2.2 Meteorological data**

202 The ground hourly data from 1980 to 2021 is collected from 5032 automated meteorological stations
 203 of airports over land. Automated surface observations reduce errors associated with human
 204 involvement in data collection, processing, and transmission. The data can be downloaded at
 205 <https://mesonet.agron.iastate.edu/ASOS>. The data is extracted from the Meteorological Terminal
 206 Aviation Routine Weather Report (METAR). The World Meteorological Organization (WMO) sets
 207 guidelines for METAR reports, including report format, encoding, observation instruments and
 208 methods used, data accuracy, and consistency. These requirements ensure consistency and
 209 comparability of METAR reports globally. International regulations can be referenced at
 210 <https://community.wmo.int/en/implementation-areas-aeronautical-meteorology-programme>.
 211 Among them, over 1,000 stations belong to the Automated Surface Observing System (ASOS), and
 212 others are sourced from airport reports around the world.

213 The daily average visibility is calculated using harmonic mean. Experiments have found that
 214 harmonic average visibility can better detect the weather phenomena than arithmetic average
 215 visibility (Noaa et al., 1998). The visibility is calculated using the extinction coefficient, which is
 216 directly proportional to the reciprocal of visibility (Wang et al., 2009). Harmonious average
 217 visibility can capture the process of visibility decline more quickly. Therefore, daily visibility will
 218 have greater representativeness:

219
$$V = n / \left(\frac{1}{V_1} + \frac{1}{V_2} + \dots + \frac{1}{V_n} \right) \tag{1}$$
 Eq.

221 where V is the harmonic mean visibility, n = 24 for the daily visibility, and V_1, V_2, \dots, V_n are the
 222 individual hourly visibility.

223 In addition to hourly visibility (VIS), other variables closely related to aerosol properties are selected,
224 including relative humidity (RH), dew point temperature (DT), temperature (TMP), wind speed
225 (WS) and sea-level pressure (SLP). Temperature affects atmospheric stability and the rate of
226 secondary particle formation, and humidity influences the size and hygroscopic growth, and wind
227 speed and pressure significantly impact the transport and deposition. Sky conditions (cloud amount)
228 and hourly precipitation are also selected to remove the records of extensive cloud cover and
229 precipitation.

230 We processed the data as follows. The records with high missing values ratio are eliminated (Husar
231 et al., 2000). When over 80% overcast or fog, the records of sky conditions are eliminated, though
232 such situations occur less than 1% of the time over land (Remer et al., 2008). The records with 1-
233 hour precipitation greater than 0.1 mm are eliminated. We calculate the temperature dew point
234 difference (dT). The low visibility records under “blowing snow” weather are eliminated at high
235 latitude region (> 65°N), when wind speed is great than 4.5m/s (Husar et al., 2000). When the RH
236 is greater than 90%, it is impossible to distinguish whether it is fog or haze, or both, and even
237 precipitation. The records with RH greater than or equal to 90% are eliminated. When the RH is less
238 than 30%, the dilution effect of aerosols is very low or even negligible. When RH is between 30%
239 and 90%, visibility is converted to dry visibility (Yang et al., 2021c):

$$240 \quad \mathbf{VISD = VIS / (0.26 + 0.4285 * \log(100 - RH))}, \quad \underline{\hspace{10em}}$$

241 (2)Eq. 2

242 where VISD is the dry visibility.

243 Daily average of variables are-is calculated by at least 3 hourly records.

244 **2.3 Boundary layer height**

245 The hourly boundary layer height (BLH) from 1980 to 2021 is available from the Fifth Generation
246 reanalysis of the European Medium-Range Weather Forecast Center (ERA5) with a resolution of
247 0.25° x 0.25° (<https://cds.climate.copernicus.eu>), which is the successor of ERA-Interim and has
248 undergone various improvements (Hersbach et al., 2020). The atmospheric boundary layer is the
249 layer closest to the Earth's surface and exhibits complex turbulence activities, and its height
250 undergoes significant diurnal variation. The effects of the boundary layer on aerosols are mainly
251 manifested in vertical distribution, concentration changes, transport, and deposition (Ackerman et
252 al., 1995). The characteristics and variations in the boundary layer play a crucial role in regulating
253 and adjusting the distribution of atmospheric aerosols. The boundary layer height serves as an
254 approximate measure of the scale height for aerosols (Zhang et al., 2020).

255 Compared to observations of 300 stations over world from 2012 to 2019, the BLH of ERA5 was
256 underestimated by 131.96m. Compared with the underestimated MERRA-2 (166.35m), JRA-55
257 (351.49m), and NECP-2 (420.86m), the BLH of ERA5 was closest to the observations (Guo et al.,
258 2021). The BLH hourly data is temporally and spatially matched with the meteorological data before
259 calculating the daily average.

260 Because the inverse of visibility is proportional to the extinction coefficient and positively related
261 to AOD (Wang et al., 2009), we calculated the reciprocal of visibility (VISI) and the reciprocal of
262 dry visibility (VISDI). Due to the influence of boundary layer height on the vertical distribution of
263 particles (Zhang et al., 2020), we calculated the product (VISDIB) of the reciprocal of dry visibility

264 and BLH. Therefore, the Predictor (Figure 2) is composed of 11 variables (TMP, Td, dT, RH, SLP,
265 WS, VIS, BLH, VISI, VISDI, and VISDIB).

266 **2.4 MODIS AOD pProducts**

267 Satellite daily AOD is available from the Moderate Resolution Imaging Spectroradiometer (MODIS)
268 Level 3 Collection 6.1 AOD products of the Aqua (MYD09CMA) satellite from 2002 to 2021 and
269 Terra (MOD09CMA) satellite from 2000 to 2021 with a spatial resolution of $0.05^\circ \times 0.05^\circ$ at a
270 wavelength of 550 nm (<https://ladsweb.modaps.eosdis.nasa.gov>). MOD/MYD09 has a higher
271 spatial resolution than MOD/MYD08 ($1^\circ \times 1^\circ$), which may result in a greater difference in AOD
272 values and reduce the proximity ratio to match the visibility-derived AOD at station scale. Terra
273 (passing approximately 10:30 am local time) and Aqua (passing approximately 1:30 pm local time)
274 were successfully launched in December 1999 and May 2002, respectively.

275 MODIS, carried on the Terra and Aqua satellites is a crucial instrument in the NASA Earth
276 Observing System program, which is designed to observe global biophysical processes
277 (Salomonson et al., 1987). The 2,330 km-wide swath of the orbit scan can cover the entire globe
278 every one to two days. MODIS has 36 channels and more spectral channels than previous satellite
279 sensors (such as AVHRR). The spectral range from 0.41 to $15\mu\text{m}$ representing three spatial
280 resolutions: 250 m (2 channels), 500 m (5 channels), and 1 km (29 channels). The aerosol retrieval
281 algorithms use seven of these channels ($0.47\text{--}2.13\mu\text{m}$) to retrieve aerosol characteristics and uses
282 additional wavelengths in other parts of the spectrum to identify clouds and river sediments.
283 Therefore, it has the ability to characterize the spatial and temporal characteristics of the global
284 aerosol field.−

285 The MODIS aerosol product actually takes use of different algorithms for deriving aerosols over
286 land and ocean. The Dark Target (DT) algorithm is applied to densely vegetated areas because the
287 surface reflectance over dark-target areas was lower in the visible channels and had nearly fixed
288 ratios with the surface reflectance in the shortwave and infrared channels (Levy et al., 2007; Levy
289 et al., 2013). The Deep Blue (DB) algorithm was originally applied to bright land surfaces (such as
290 deserts), and later extended to cover all cloud-free and snow-free land surfaces (Hsu et al., 2006;
291 Hsu et al., 2013). MODIS Collection 6.1 aerosol product was released in 2017, incorporating
292 significant improvements in radiometric calibration and aerosol retrieval algorithms.−

293 The expected errors are $\pm (0.05 \pm 15\%)$ for the DT retrievals over land. Higher spatial coverage is
294 observed in August and September, reaching 86-88%. During December and January, due to the
295 presence of permanent ice and snow cover in high-latitude regions of the Northern Hemisphere, the
296 spatial coverage is 78-80%. Thus, challenges remain in retrieving AOD values in high-latitude
297 regions (Wei et al., 2019). However, visibility observations are available in high-latitude regions,
298 thereby partially addressing the lack in these regions.

299 In this study, the Terra and Aqua MODIS AOD are temporally and spatially matched with the
300 meteorological stations. Aqua MODIS AOD is used as the Target, when training the model, and
301 Terra MODIS AOD is used in the evaluation and validation of the model results, as shown in the
302 flowchart (Figure 2).

303 **2.5 Ground-based AOD**

304 Ground-based 15-minute AOD data are available from the Aerosol Robotic Network (AERONET)
305 Version 3.0 Level 2.0 product at 395 [stations-sites](#) (Figure 1), which can be downloaded from

306 <https://aeronet.gsfc.nasa.gov>. The AERONET program is a federation of ground-based remote
 307 sensing aerosol networks established by NASA and PHOTONS, including many subnetworks (such
 308 as AeroSpan, AEROCAN, NEON, and CARSNET). The sun photometer (CE-318) measures
 309 spectral sun and sky irradiance in the 340-1020 nm spectral range. When the aerosol loading is low,
 310 the error is significant. When the AOD at 440 nm wavelength is less than 0.2, the error is 0.01,
 311 which is equivalent to the error of the absorption band in the total optical depth (Dubovik et al.,
 312 2002a). The total uncertainty in AOD under cloud-free conditions is less than ± 0.01 for wavelength
 313 more than 440 nm, and ± 0.02 for wavelength less than 440 nm (Holben et al., 1998). AERONET
 314 has three levels of AOD products: Level 1.0 (unscreened), Level 1.5 (cloud screened), and Level
 315 2.0 (cloud screened and quality assured). Compared to Version 2, the Version 3 Level 2.0 database
 316 has undergone further cloud screening and quality assurance, which is generated based on Level 1.5
 317 data with pre- and post-calibration and temperature adjustment and is recommended for formal
 318 scientific research (Giles et al., 2019). AERONET provides AOD products at wavelengths of 440,
 319 675, 870, and 1020 nm. The AOD at 440nm and the Ångström index at 440-675nm are used for
 320 AOD at 550 nm not provided by AERONET, as shown in Eq. 3(3). AERONET AOD, as the ‘true’
 321 value, is the average of at least two times within 1 hour (± 30 minutes) of Aqua transit time (Wei et
 322 al., 2019):—

$$\tau_{550} = \tau_{440} \left(\frac{550}{440} \right)^{-\alpha}$$

(3)Eq. 3

325 where τ_{440} and τ_{550} are the AOD at a wavelength of 440nm and 550 nm, and α is the Ångström
 326 index.

327 The matching conditions between AERONET sites and meteorological stations are (1) a distance of
 328 less than 0.5° (2) at least three years of observation. Finally, a total of 395 pairs were matched.

2.6 AOD reanalysis dataset

330 The monthly AOD (550nm) dataset of Modern-Era Retrospective Analysis for Research and
 331 Applications version 2 (MERRA-2) from 1980 to 2021 is a NASA reanalysis of the modern satellite
 332 era produced by NASA’s Global Modeling and Assimilation Office with a spatial resolution of
 333 $0.5 \times 0.625^\circ$ (Gelaro et al., 2017), available at <https://disc.gsfc.nasa.gov>. MERRA-2 AOD uses an
 334 analysis splitting technique to assimilate AOD at 550 nm. AOD observations are including (1)
 335 AOD retrievals –from AVHRR (1979-2002) over global ocean, (2) AOD retrievals from MODIS
 336 on Terra (2000–present) and Aqua (2002–present) over global land and ocean, (3) AOD retrievals
 337 from MISR (2000–2014) over bright and desert surfaces, and (4) direct AOD measurements from
 338 the ground-based AERONET (1999–2014) (Gelaro et al., 2017). The monthly MERRA-2 AOD is
 339 used to evaluate the model’s predictive ability before 2000 and after 2000.

2.76 Decision tFree rRegression

2.76.1 Feature selection

342 Although a multidimensional dataset can provide as much potential information as possible for
 343 AOD, irrelevant and redundant variables can also introduce significant noise in the model and
 344 reduce the model’s accuracy and stability (Kang et al., 2021; Dong et al., 2023). Therefore, the F-

345 test is used to search for the optimal feature subset in the Predictor, aiming to eliminate irrelevant
346 or redundant features and select truly relevant features, which helps to simplify the model's input
347 and improve the model's prediction ability (Dhanya et al., 2020). The F-test is a statistical test that
348 gives an f-score($-\log(p)$, p represents the degree to which the null hypothesis is not rejected) by
349 calculating the ratio of variances. In this study, we calculate the ratio of variance between the
350 Predictors and Target, and the features are ranked based on higher values of the f-score. A greater
351 value of f-score means that the distances between Predictors and Target are less and the relationship
352 is closer, thus, the feature is more important. We set $p=0.05$. When the score is less than $-\log(0.05)$,
353 the variable in the Predictors is not considered.-

354 **2.76.2 Data balance**

355 When it is clear, the AOD value is small, the variability of AOD is small ($AOD < 0.5$), and the data is
356 concentrated near the mean value. When heavy pollution, the AOD value is large ($AOD > 0.5$). Compared
357 to clear sky, the AOD sequence will show "abnormal" large values with low frequency, which is the
358 imbalance of AOD data. When dealing with imbalanced datasets, because of the tendency of machine
359 learning algorithms to perform better on the majority class and overlook the minority class, the model
360 can be underfit (Chuang and Huang, 2023). Data augmentation techniques are commonly employed to
361 address the issue in imbalance data, which applies a series of transformations or expansions to generate
362 new training data, thereby increasing the diversity and quantity of the training data.

363 The Adaptive Synthetic Sampling (ADASYN) is a data augmentation technique specifically designed to
364 address data imbalance problem (He et al., 2008; Mitra et al., 2023). It is an extension of the Synthetic
365 Minority Over-sampling Technique (SMOTE) algorithm (Fernández et al., 2018). The goal of ADASYN
366 is to generate synthetic sample data for the minority class to increase its representation in the dataset.
367 ADASYN, which adaptively adjusts the generation ratio of synthetic samples based on the density
368 distribution of sample data, improves the dataset balance and enhances the performance of machine
369 learning models in dealing with imbalanced data.

370 The processing of imbalanced data includes (1) AOD sequences are classified into three types based on
371 percentile (0-1%, 2% -98%, 99%), (2) When the mean of the third type of AOD is greater than 5 times
372 the standard bias of the second type, it is considered an imbalanced sequence. These data, with a total
373 amount less than 5% of the sample, are imbalanced data, and (3) Then synthetic samples are generated
374 with the upper limit 10% of the samples.

375 **2.76.3 Decision tFree rRegression mModel**

376 The decision tree is a machine learning algorithm based on a tree-like structure used to solve
377 classification and regression problems. We adopt the CART algorithm to construct a regression tree by
378 analyzing the mapping relationship between object attributes (Predictors) and object values (Target). The
379 internal nodes have binary tree structures with feature values of "yes" and "no". In addition, each leaf
380 node represents a specific output for a feature space. The advantages of the regression tree include the
381 ability to handle continuous features and the ease of understanding the generated tree structure (Teixeira,
382 2004; Berk, 2008). Before training the tree model, the variables (Input) are normalized to improve model
383 performance, and after prediction, the results are obtained by denormalization. The 10-fold cross-
384 validation method is employed to improve the generalization ability of the model (Browne, 2000).

385 The core problems of the regression tree need to be solved are to find the optimal split variable and

386 optimal split point. The optimal split point of Predictors is determined by the minimum MSE, which in
 387 turn determines the optimal tree structure. We set $Y = [y_1, y_2, \dots, y_N]$ as the Target. We set $X =$
 388 $[x_1, x_2, \dots, x_N]$ as the Predictors, $x_i = (x_i^1, x_i^2, \dots, x_i^n)$, $i = 1, 2, 3, \dots, N$, where n is the feature number, and
 389 N is the length of sample. We set a training dataset as $D = [(x_1, y_1), (x_2, y_2), \dots, (x_N, y_N)]$.

390 A regression tree corresponds to a split in the feature space and the output values on the split domains.
 391 Assuming that the input space has been divided into M domains $[R_1, R_2, \dots, R_M]$ and there is a fixed
 392 output value on each R_M domain, the regression tree model can be represented as follows:

$$393 \quad f(x) = \sum_{m=1}^M c_m I(x \in R_m), m = 1, 2, \dots, M, \quad \text{Eq.} \\
 394 \quad \mathbf{4(4)}$$

395 where I is the indicator function, (Eq. (5)5):

$$396 \quad I = \begin{cases} 1, & x \in R_m \\ 0, & x \notin R_m \end{cases} \quad \text{Eq.} \\
 397 \quad \mathbf{5(5)}$$

398 When the partition of the input space is determined, the square error can be used to represent the
 399 prediction error of the regression tree for the training data, and the minimizing square error is used to
 400 solve the optimal output value on each domain. The optimal value (\widehat{c}_m) on a domain is the mean of the
 401 outputs corresponding to all input, namely:

$$402 \quad \widehat{c}_m = \text{ave}(y_i | x_i \in R_m), \quad \text{Eq.} \\
 403 \quad \mathbf{6(6)}$$

404 A heuristic method is used to split the feature space in CART. After each split, all values of all features
 405 in the current set are examined individually, and the optimal one is selected as the split point based on
 406 the principle of minimum sum of the square errors. The specific step is described as follows: for the
 407 training dataset D , we recursively divide each region into two sub domains and calculate the output
 408 values of each sub domain; then, construct a binary decision tree. For example, split variable is x^j and
 409 split point is s . Then, in the domain $R_1(j, s) = [x | x^j \leq s]$ and domain $R_2(j, s) = [x | x^j > s]$, we can
 410 solve the loss function $L(j, s)$ to find the optimal j and s .

$$411 \quad L(j, s) = \sum_{x_i \in R_1(j, s)} (y_i - c_1)^2 + \sum_{x_i \in R_2(j, s)} (y_i - c_2)^2, \quad \text{Eq.} \\
 412 \quad \mathbf{7(7)}$$

413 When $L(j, s)$ is the smallest, x^j is the optimal split variable and s is the optimal split point for the
 414 x^j .

$$415 \quad \min_{j, s} \left[\min_{c_1} \sum_{x_i \in R_1(j, s)} (y_i - c_1)^2 + \min_{c_2} \sum_{x_i \in R_2(j, s)} (y_i - c_2)^2 \right], \quad \text{Eq.} \\
 416 \quad \mathbf{8(8)}$$

417 We use the optimal split variable x^j and the optimal split point s to split the feature space and calculate
 418 the corresponding output value.

$$419 \quad \widehat{c}_1 = \text{ave}(y_i | x_i \in R_1(j, s)), \quad \widehat{c}_2 = \text{ave}(y_i | x_i \in R_2(j, s)), \quad \text{Eq.} \\
 420 \quad \mathbf{9(9)}$$

421 We traverse all input variables to find the optimal split variable x^j , forming a pair (j, s) . Divide the
 422 input space into two regions accordingly. Next, repeat the above process for each region until the stop
 423 condition is met. The regression tree is generated.

424 Therefore, the regression tree model $f(x)$ can be represented as follows:

$$425 \quad f(x) = \sum_{m=1}^M \widehat{c}_m I(x \in R_m), m = 1, 2, \dots, M, \quad \text{Eq. 10(10)}$$

427 2.87 Gridding method

428 Kriging is a regression algorithm to model and predict (interpolate) random processes/fields based on the
 429 covariance function, which is widely used in geo-statistics (Pebesma, 2004). Ordinary Kriging is the
 430 earliest and most extensively studied form of Kriging. It is a linear estimation system applicable to any
 431 intrinsic stationary random field that satisfies the assumption of isotropy. The two key parameters of
 432 Ordinary Kriging are the semi-variogram function and the weight factors (Goovaerts, 2000). It has been
 433 widely applied in fields, such as climatology, environmental science, and agriculture (Lapen and Hayhoe,
 434 2003; Chen et al., 2010), due to high accuracy, stability, and insensitivity to data shape and distribution.
 435 This study utilizes area-weighted ordinary kriging algorithm to estimate the unknown values of AOD at
 436 specific locations to generate gridded AOD. The longitude range is between -179.5° E and 180° E, the
 437 latitude range is between -60° N and 85° N, and the spatial resolution is $0.5^\circ \times 0.5^\circ$.

438 Kriging variance represents the spatial correlation between different points, which is calculated by the
 439 semi variogram function (Goovaerts, 2000). Kriging variance is used to assess the spatial uncertainty of
 440 interpolation results, indicating the difference between predicted and true values. A higher kriging
 441 variance indicates fewer neighboring points and greater uncertainty, while a lower variance implies less
 442 uncertainty. To quantify the uncertainty of interpolation results, we provide the width of the confidence
 443 interval under the 95% confidence level based on kriging variance (Van Der Veer et al., 2009).

444 2.89 Evaluation metrics

445 Evaluation metrics, including Root Mean Squared Error (RMSE), Mean Absolute Error (MAE) and
 446 Pearson Correlation Coefficient (R), are used to measure the performance and accuracy of the model and
 447 gridded results.

$$448 \quad RMSE = \sqrt{\frac{1}{n} \sum_{i=1}^n (y_i - \widehat{y}_i)^2}, \quad \text{Eq. 11(11)}$$

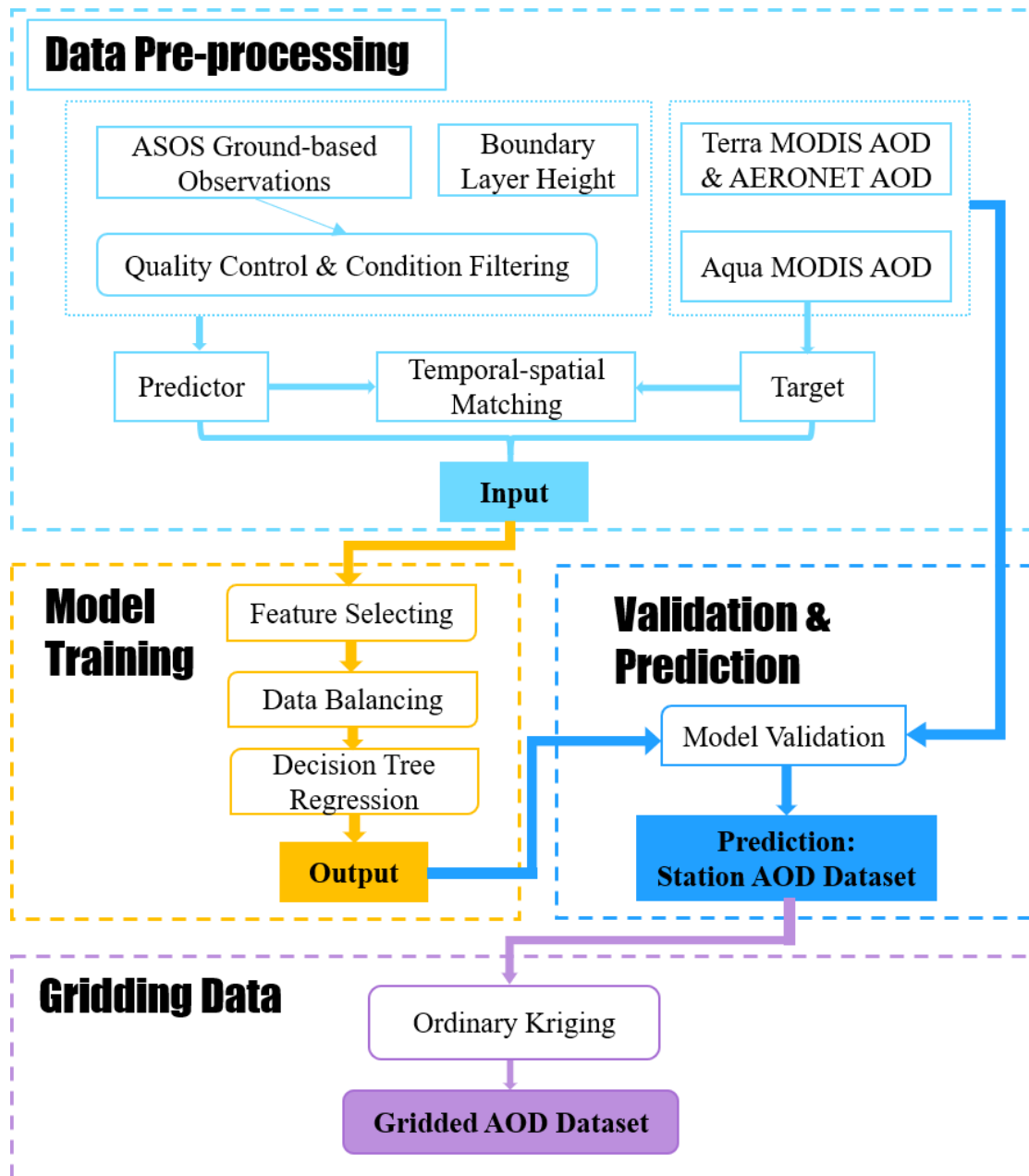
$$450 \quad MAE = \frac{1}{n} \sum_{i=1}^n |y_i - \widehat{y}_i|, \quad \text{Eq. 12(12)}$$

$$452 \quad R = \frac{\sum_{i=1}^n (y_i - \bar{y})(\widehat{y}_i - \bar{\widehat{y}})}{\sqrt{(\sum_{i=1}^n (y_i - \bar{y})^2)(\sum_{i=1}^n (\widehat{y}_i - \bar{\widehat{y}})^2)}}, \quad \text{Eq. 13(13)}$$

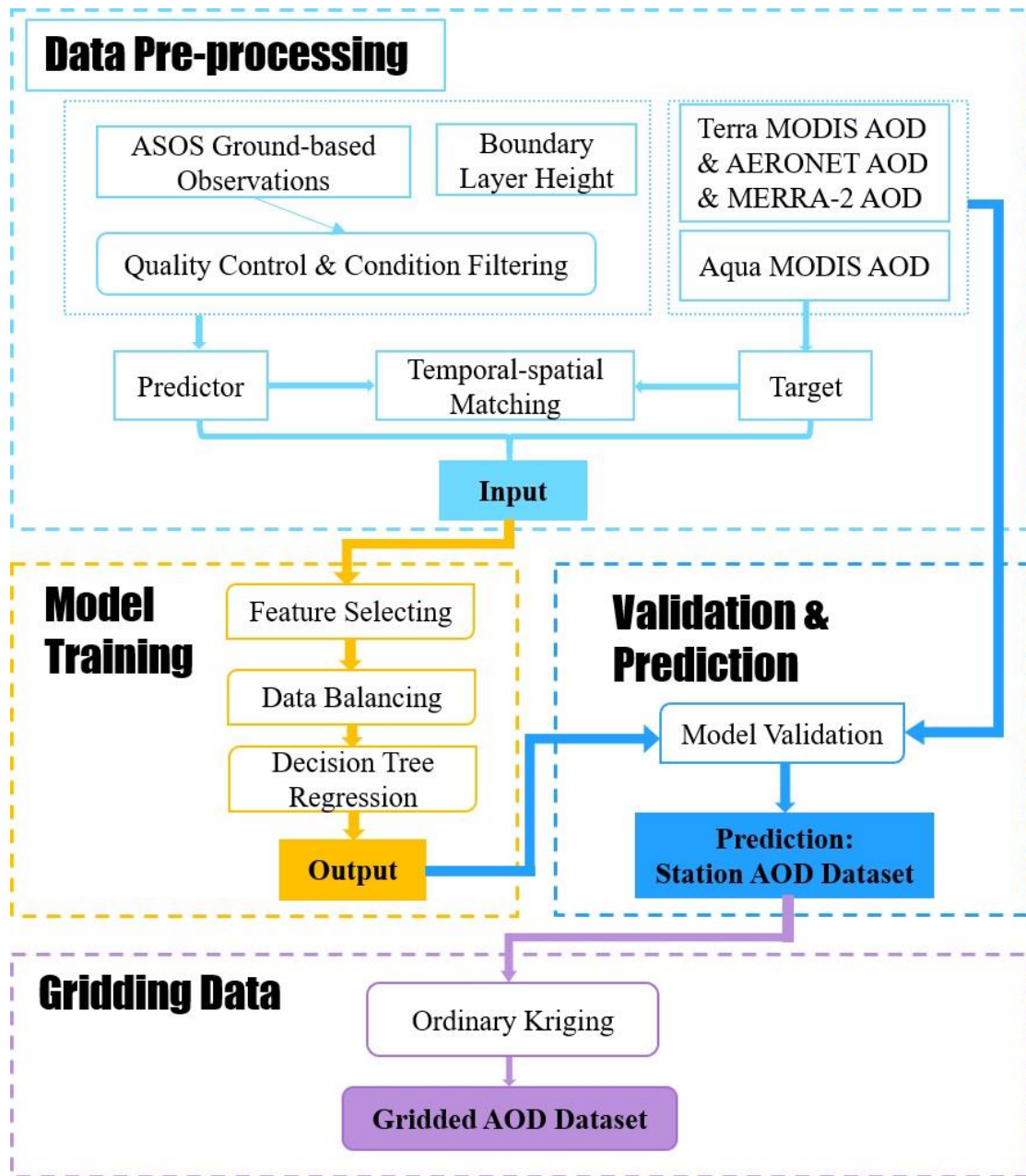
454 where y_i and \bar{y} are the predicted value and the average of the predicted values. \widehat{y}_i and $\bar{\widehat{y}}$ are
 455 the target and the average of the target. $i = 1, 2, \dots, n$. n is the length of sample.

456 The expected error (EE) is used to evaluate the AOD derived from visibility.

457 $EE = \pm(0.05 + 0.15 * \tau_{targettrue})$ _____
 458 -Eq.14(14)
 459 where $\tau_{targettrue}$ is the AOD at 550 nm from AERONET, satellite and reanalysis datasets. AOD
 460 or Terra MODIS AOD at 550nm.
 461 The width of 95% confidence interval (CI) is calculated from the kriging variance (s^2) (Van Der Veer et
 462 al., 2009) ;
 463 $95\% \text{ CI} = 1.96 * \sqrt{s^2}$, _____ (15)



464



465

466 **Figure 2:** Flowchart for deriving aerosol optical depth (AOD).

467

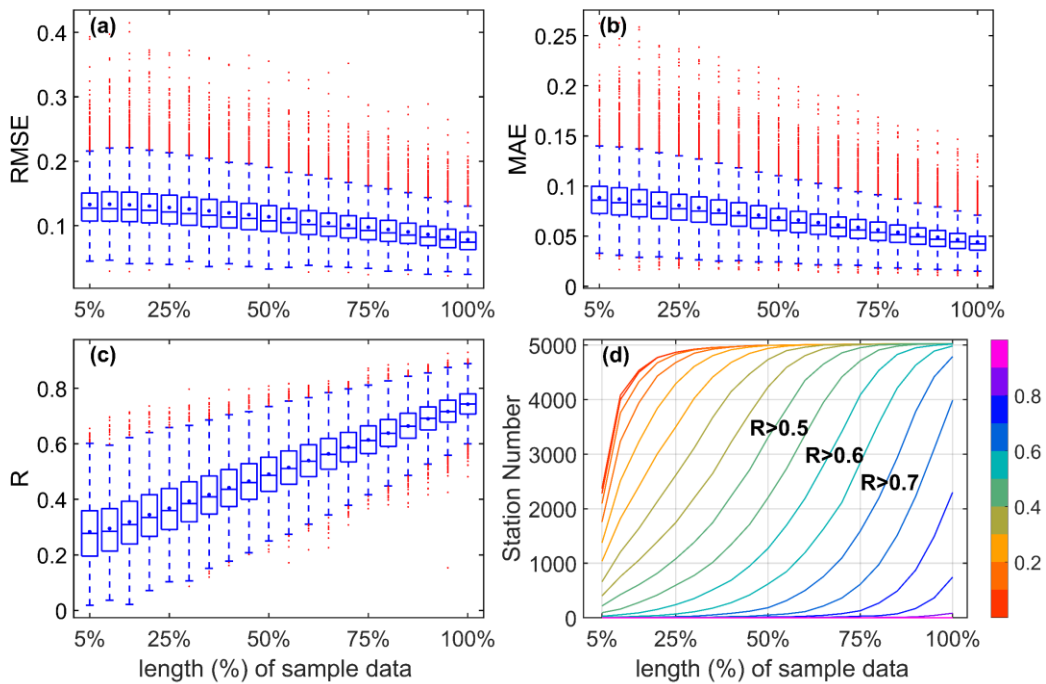
468 **2.109 Workflow**

469 Figure 2 ~~is the~~ summarizes ~~the~~ flowchart and provides an overview of the structure of this study,
 470 which involves four main parts: (1) data preprocessing, (2) model training, (3) validation and
 471 prediction, and (4) data gridding.

472 **3 Results and discussion**

473 **3.1 Dependence of model performance on training data length**

474



475

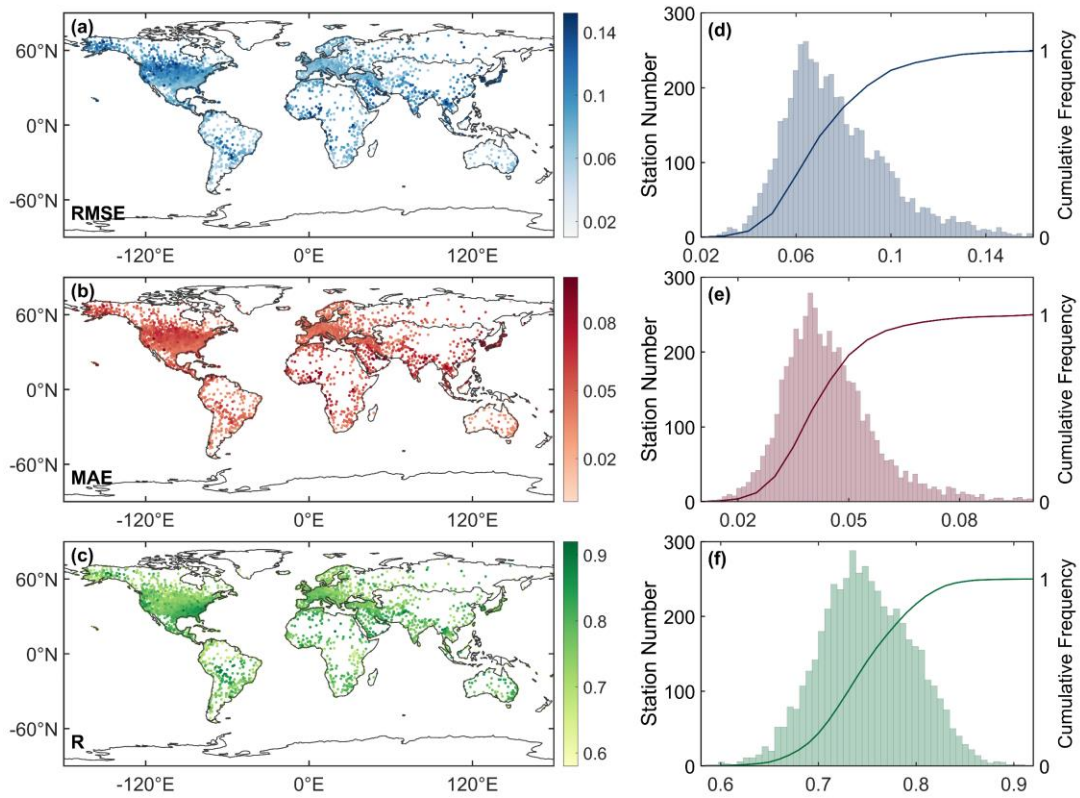
476 **Figure 3:** Boxplots of root mean squared error (RMSE) (a), mean absolute error (MAE) (b), and
 477 correlation coefficient (R) (c) between predicted values and target using different lengths of sample
 478 data (5% interval) as the training dataset, and the correlation coefficient curve (d) of the station
 479 number in the different lengths of sample data.

480 We build the models using different lengths of sample data (5% to 100%, with a 5% interval) by random
 481 allocation without overlap and evaluate the predictive performance of each model. Figure 3 depicts
 482 RMSE(a), MAE(b), and R (c) between the predicted values and target based on the training data of 5%
 483 to 100% sample data at a station. As the volume of the training data increases, the RMSE and MAE
 484 decrease, and the correlation coefficient increases. Compared to 5% of the sample data, the result of 100%
 485 sample data shows a decrease in RMSE by 41.1%, a decrease in MAE by 50.1%, and an increase in R
 486 by 162.3%. The relationship between the length of sample data and the model's performance is positive
 487 for each station. Figure 3 (d) shows that R of approximately 70% stations is greater than 0.5 at 50% of
 488 the sample data, while at 75%, the R of approximately 80% of stations is greater than 0.6. When 100%
 489 of the sample data is used as sample data, the R of approximately 80% of stations is greater than 0.75,
 490 and the R of about 97% is greater than 0.7. This finding indicates that the predictive capability and
 491 robustness of the model increase as the amount of training data increases. It may be attributed to the
 492 model's ability to capture more complex patterns and relationships among the input by multi-year data.

493 3.2 Evaluation of model training

494 Figure 4 shows the spatial distribution (a-c) and frequency and cumulative frequency (d-e) of RMSE,
 495 MAE, and R of all stations. The mean values of RMSE, MAE, and R are 0.078, 0.044, and 0.750,
 496 respectively. The RMSE of 93% stations is less than 0.11, the MAE of 91% is less than 0.06, and the R
 497 of 88% is greater than 0.7. The R values in Africa, Asia, Europe, North America, Oceania, and South
 498 America are 0.763, 0.758, 0.736, 0.750, 0.759, and 0.738, respectively. Although the RMSE and MAE
 499 of a few stations are high in America and Asia, the R is still high (>0.6). Therefore, the results of the

500 model's errors demonstrate that the model performs well on almost all stations.



501

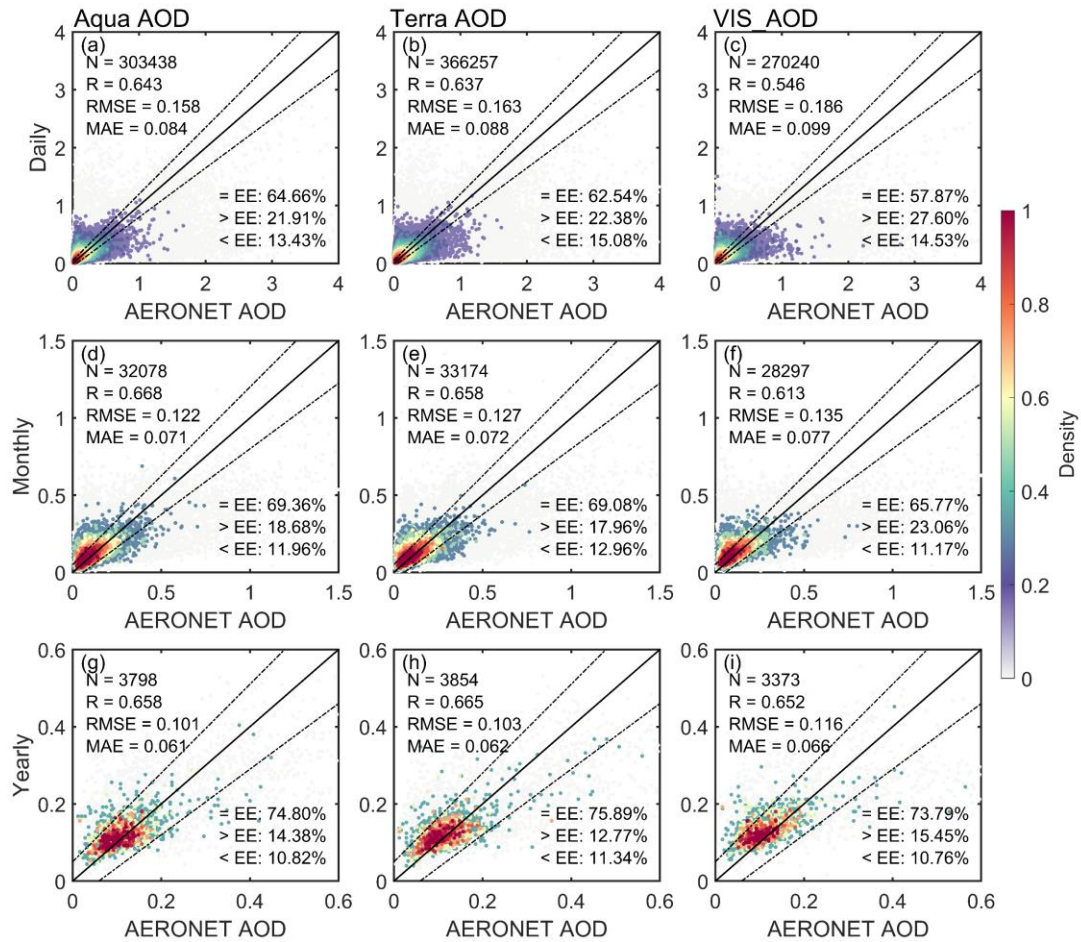
502 **Figure 4:** Spatial distribution (a-c) of root mean squared error (RMSE), mean absolute error (MAE),
503 and correlation coefficient(R) between the model's result and target with 100% sample data. Station
504 number (bar) and cumulative frequency (curve) (d-e) of RMSE, MAE, and R.

505 3.3 Validation and comparison with MODIS and AERONET AOD

506 3.3.1 Validation over global land

507 To validate the model's predictive ability, the visibility-derived AOD (for short, VIS_AOD) is compared
508 with Aqua, Terra and AERONET AOD at 550nm for the global scale. Among them, Aqua AOD has been
509 used as training data, which is not independent. Terra AOD and AERONET AOD have not been used as
510 training data and can be regarded as independent data.

511 First, the relationship among daily MODIS and AERONET AOD is evaluated. Figure 5 shows the scatter
512 density plots between AERONET AOD and Aqua AOD (a, d, g) and Terra AOD (b, e, h). The R values
513 with Aqua AOD and Terra AOD are 0.643 and 0.637 on the daily scale, and 0.668 and 0.658 on the
514 monthly scale, 0.658 and 0.665 on the yearly scale. The RMSE with Aqua AOD and Terra AOD are 0.158
515 and 0.163 on the daily scale, and 0.122 and 0.127 on the monthly scale, 0.101 and 0.103 on the yearly
516 scale. The MAE values with Aqua AOD and Terra AOD are 0.084 and 0.088 on the daily scale, and 0.071
517 and 0.072 on the monthly scale, 0.061 and 0.062 on the yearly scale. The percentages of sample point
518 falling within the EE envelopes are 64.66% and 62.54% on the daily scale, and 69.36% and 69.08% on
519 the monthly scale, 74.80% and 75.89% on the yearly scale.



520

521 **Figure 5:** Scatter density plots between AERONET AOD (550nm) and Aqua MODIS AOD, Terra
 522 MODIS AOD and VIS_AOD ~~on~~ the daily (a-c), monthly (d-f) and yearly (g-i) scale. The solid black
 523 line represents the 1:1 line and the dashed lines represents expected error (EE) envelopes. The sample
 524 size (N), correlation coefficient (R), mean absolute error (MAE), and root mean square error (RMSE)
 525 are given. ‘=EE’, ‘>EE’, and ‘<EE’ represent the percentages (%) of retrievals falling within, above,
 526 and below the EE, respectively. The matching time for Aqua AOD and VIS_AOD with AERONET AOD
 527 is 13.30 (\pm 30 minutes) at local time, and the matching time between Terra AOD and AERONET AOD
 528 is 10.30 (\pm 30 minutes) at local time.

529 Figure 6 shows the scatter density plots and the EEs between VIS_AOD and Aqua AOD, Terra AOD,
 530 and AERONET AOD. Aqua AOD is not an independent validation, and Terra and AERONET AOD are
 531 independent validation. For the daily scale, the R, RMSE and MAE of between VIS_AOD and Aqua
 532 AOD (15,962,757 pairs data) is 0.799, 0.079 and 0.044, respectively. The percentage of sample point
 533 falling within the EE envelopes is 84.12% on the global scale (Figure 6 a). The R between VIS_AOD
 534 and Terra AOD (17,145,578 pairs data) is 0.542, with a RMSE of 0.125 and MAE of 0.078. The
 535 percentage falling within the EE envelopes is 64.76% (Figure 6 b). The R between VIS_AOD and
 536 AERONET AOD (270,240 pairs data) at 3957 sites is 0.546, with a RMSE of 0.186 and MAE of 0.099.
 537 The percentage falling within the EE envelopes is 57.87% (Figure 6 c).

538 For the monthly and annual scales, RMSE and MAE show a significant decrease between VIS_AOD and
 539 Aqua, Terra, and AERONET AOD, and R and percentages falling within EE show a significant increase

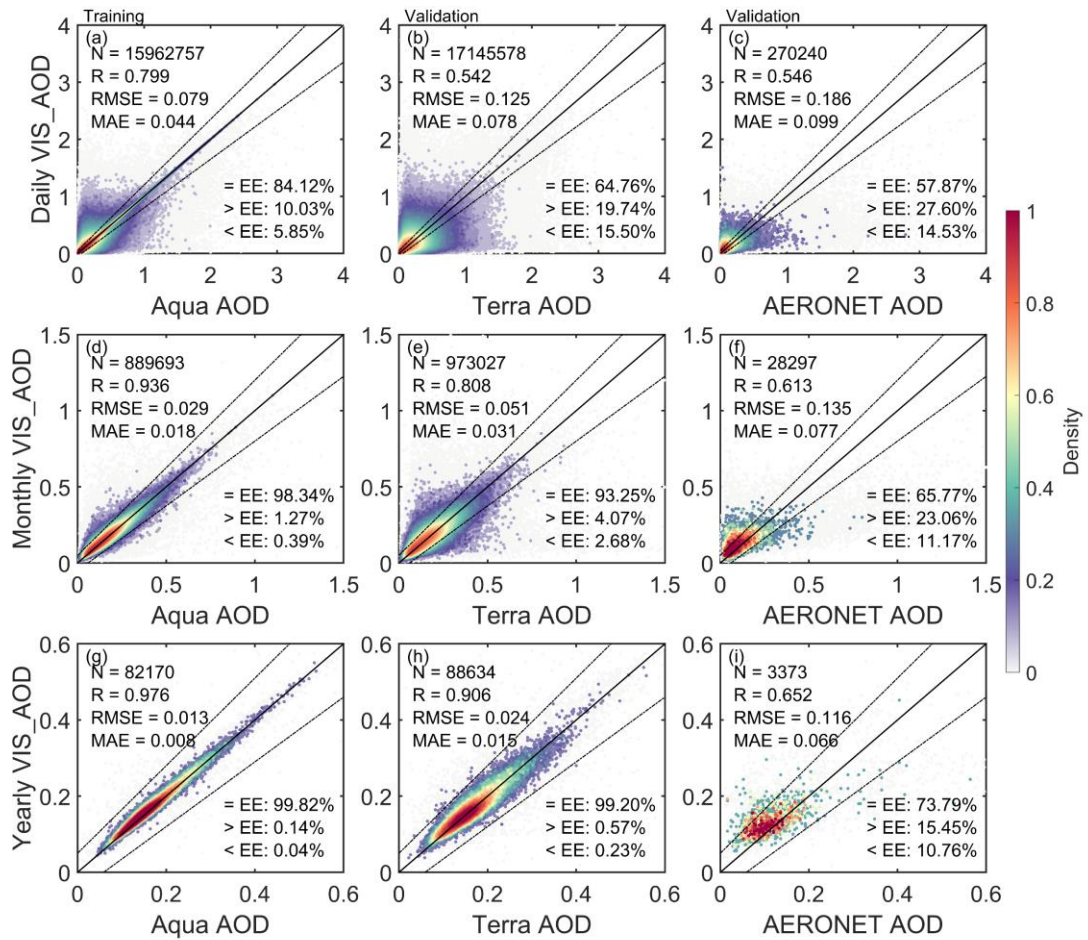
540 in Figure 6 (~~ed-g, i-ki~~). The monthly RMSEs are 0.029, 0.051, and 0.135, the monthly MAEs are 0.018,
541 0.031, and 0.077, and the R values are 0.936, 0.808, and 0.613, respectively. The percentages falling
542 within the EE envelopes are 98.34%, 93.25%, and 65.77%. The RMSEs at the annual scale are 0.013,
543 0.024, and 0.116, the MAEs are 0.008, 0.015, and 0.066, and the R values are 0.976, 0.906, and 0.652,
544 respectively. The percentages falling within the EE envelopes are 99.82%, 99.20%, and 73.79%. The
545 percentage falling within the EE envelopes against AERONET is smaller than that against Terra, which
546 may be related to the elevation of AERONET sites, the distance between AERONET and meteorological
547 stations, and observed time. The results highlighted above demonstrate a clear improvement in
548 performance on the monthly and annual scales compared to the daily scale (Schutgens et al., 2017), which
549 provided a foundation for the gridded dataset.

550 To further examine the predictive capability of historical data, we compare the VIS_AOD with
551 AERONET AOD before 2000, as shown in Figure 6 (d, h, l). We match 43 AERONET sites, with a total
552 of 5166 daily records. The result indicates that the daily-scale R is close to that after 2000 (Figure 6 c),
553 with the percentages approaching 50% falling within the EE envelopes. The monthly and annual
554 correlation coefficients are even higher, with a percentage of 55% falling within the EE envelopes.
555 Although the sample size is small, it still demonstrates the excellent predictive ability of the model.
556 Compared with AERONET (an independent validation dataset), the performance of VIS_AOD is almost
557 unchanged before and after 2000.

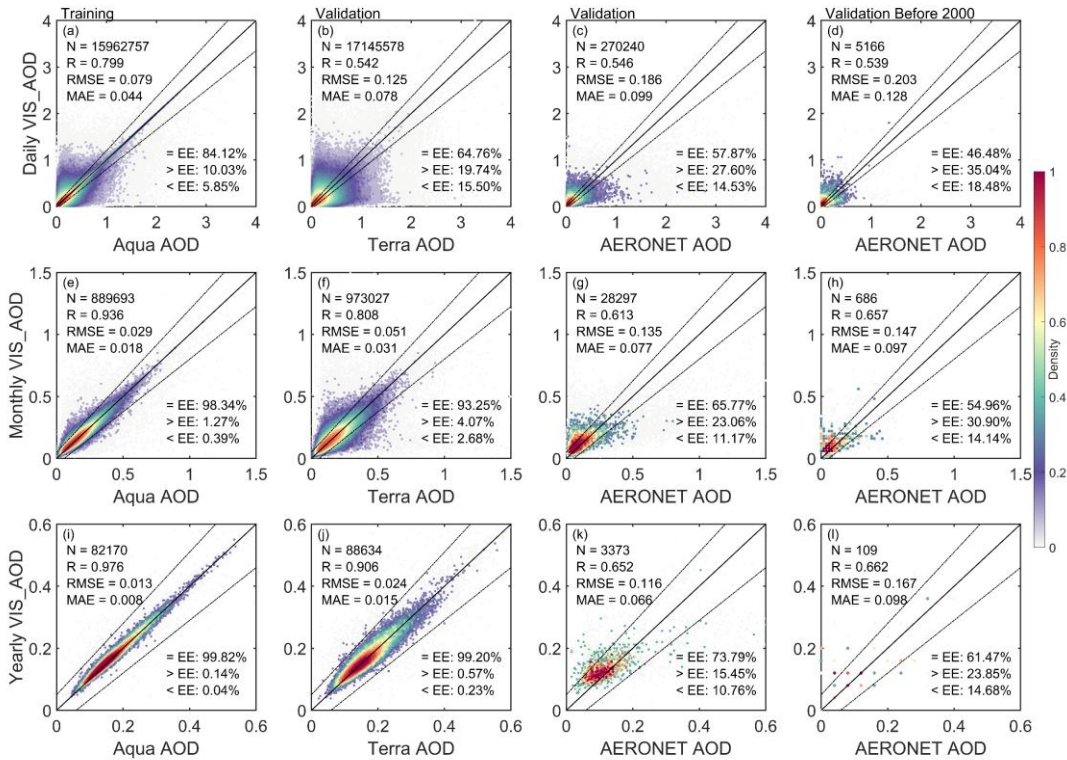
558 We also compare the VIS_AOD with the MERRA-2 reanalysis AOD on the monthly scales, as shown in
559 Figure 7. The correlation coefficient between MERRA-2 and AERONET is 0.655 before 2000, slightly
560 lower than the correlation coefficient (0.657) between VIS_AOD and AERONET. The correlation
561 coefficient between MERRA-2 and AERONET is 0.829 after 2000, significantly higher than that before
562 2000, while the correlation coefficient between VIS_AOD and AERONET is 0.613. It suggests that
563 VIS_AOD and MERRA-2 AOD have similar accuracy before 2000. The correlation of MERRA-2 after
564 2000 is higher and even performs better than MODIS retrievals (as shown in Figure 5) when evaluated
565 at AERONET sites. However, before 2000, the correlation coefficient of MERRA-2 and AERONET,
566 RMSE, and MAE all show significant changes and differences in consistency. The higher correlation
567 between MERRA-2 and AERONET AOD is partly because MERRA-2 has assimilated AERONET AOD
568 observations (Gelaro et al., 2017). Compared to AERONET, VIS_AOD and Aqua/Terra MODIS have a
569 similar correlation coefficient. The correlation coefficient of VIS_AOD before 2000 is even higher than
570 after 2000, and the changes in RMSE and MAE are not significant. It indicates good consistency of
571 VIS_AOD.

572 ~~On the daily, monthly, and annual scales, compared with AERONET AOD, the correlation coefficients,~~
573 ~~RMSE, MAE, and percentages falling within the expected error of VIS_AOD and MODIS AOD are very~~
574 ~~close. Since the time of AERONET AOD and VIS_AOD overlaps before 2000, it indicates that~~
575 ~~VIS_AOD also has the same accuracy.~~

576 In conclusion, the predicted results have good consistency with AERONET AOD and Terra AOD on the
577 daily scale. The monthly and annual results have a significant improvement. The model shows good
578 predictive capabilities before/after 2000, highlighting the stable accuracy of VIS_AOD.



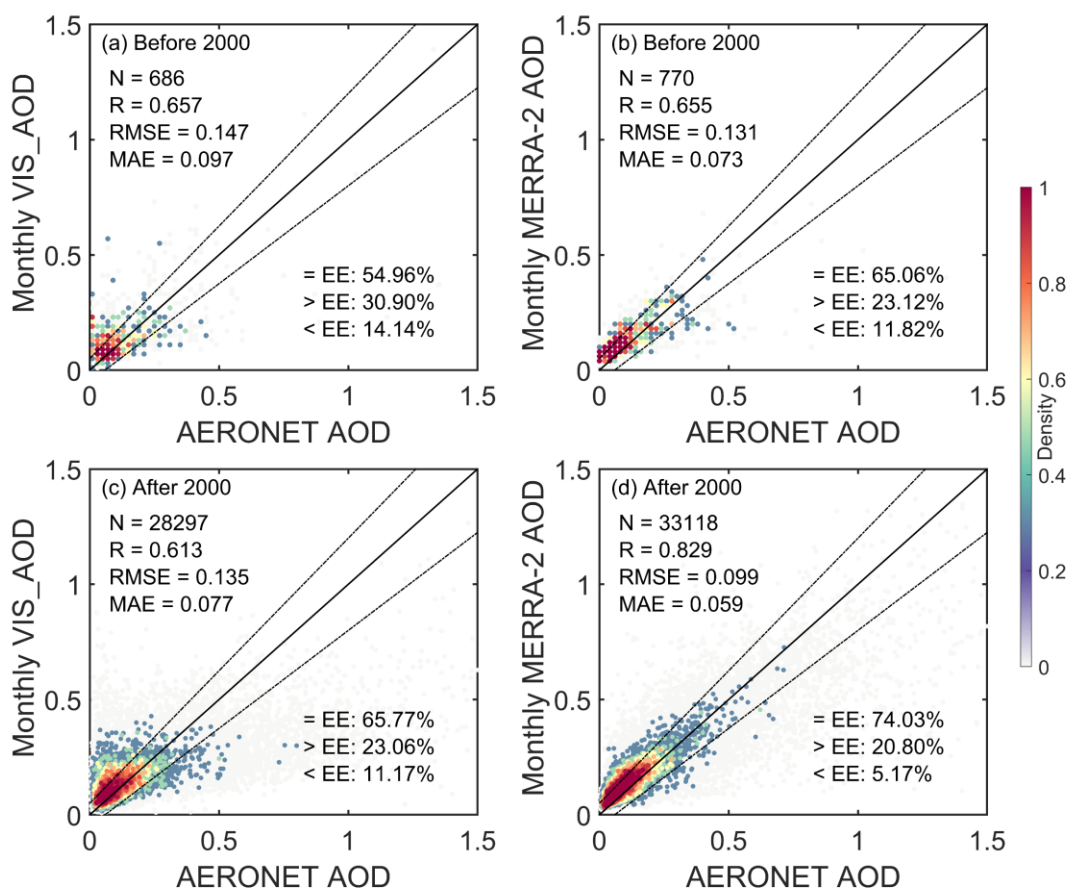
579



580

581 **Figure 6:** Scatter density plots between predicted AOD (VIS_AOD) and Aqua MODIS AOD, Terra

582 MODIS AOD, ~~and~~ AERONET AOD and AERONET AOD before 2000 on the daily (a-de), monthly
 583 (e-h) and yearly (g-i) scale. The solid black line represents the 1:1 line and the dashed lines represents
 584 expected error (EE) envelopes. The sample size (N), correlation coefficient (R), mean absolute error
 585 (MAE), and root mean square error (RMSE) are given. ‘= EE’, ‘> EE’, and ‘< EE’ represent the
 586 percentages (%) of retrievals falling within, above, and below the EE, respectively. Note Aqua AOD is
 587 not an independent validation for predicted results, while Terra and AERONET are independent
 588 validation.



589
 590 **Figure 7:** Scatter density plots between AERONET AOD and the predicted AOD (VIS_AOD) and
 591 MERRA-2 AOD before/after 2000 on the monthly scale. The solid black line represents the 1:1 line and
 592 the dashed lines represents expected error (EE) envelopes. The sample size (N), correlation coefficient
 593 (R), mean absolute error (MAE), and root mean square error (RMSE) are given. ‘= EE’, ‘> EE’, and ‘<
 594 EE’ represent the percentages (%) of retrievals falling within, above, and below the EE, respectively.

595 3.3.2 Validation over regions

596 Aerosol loading exhibits spatial variability. Evaluation metrics for the relationships between
 597 visibility-derived AOD and AERONET AOD and Terra AOD for each region are listed in Table 1.
 598 Over Europe and North America, the results are similar to those of Terra and AERONET, with a
 599 large number of data pairs, greater than 10^5 (AERONET) and greater than 10^7 except for Eastern
 600 Europe (Terra) on the daily scale. Approximately 63% -70% fall within the EE envelopes. The

601 RMSE is approximately 0.1100, except for western North America, the MAE is approximately
602 0.0700, with a correlation coefficient between 0.44 and 0.54.

603 Over Central South America, South Africa, and Australia, data pairs are about 10^{3-4} (AERONET)
604 and 10^6 (Terra) on the daily scale. 52-60% fall within the EE envelopes compared to AERONET,
605 and 58-67% compared to Terra. The RMSE is 0.03-0.05 compared to Terra, and 0.11-0.17 compared
606 to AERONET. The correlation coefficient ranges from 0.4 to 0.74, with the highest correlation
607 coefficient in South America at 0.740.

608 In Asia, India, and West Africa, the data pairs are only approximately 10^4 (AERONET). 32% to 50%
609 fall within the EE envelopes compared to AERONET, the RMSE ranges from 0.2 to 0.5, and the
610 MAE ranges from 0.11 to 0.36. 51 to 58%, compared to Terra, fall within the EE envelopes, the
611 RMSE is around 0.16, and the MAE is around 0.11. Compared to AERONET, in these high aerosol
612 loading regions, RMSE and MAE increase, and the percentages falling within the EE envelopes
613 decrease, but the correlation coefficients do not significantly decrease.

614 Compared to Terra AOD, 55% -67% of data falls within the EE envelopes on the daily scale, 87% -
615 96% on the monthly scale, and over 97% on the yearly scale. Compared to AERONET AOD, 32-
616 68% of data falls within the EE envelopes, 24% -84% on the monthly scale, and 15% -97% on the
617 yearly scale. On both monthly and yearly scales, all metrics have shown a significant increase in
618 performance when compared to Terra. However, compared to AERONET, not all metrics increase
619 in some regions due to limited data pairs, such as West Africa, Northeast Asia, and India, which may
620 be due to the spatial differences between AERONET sites and meteorological stations.

621 ~~Overall, the AOD from visibility is more effective in regions such as Europe and North America,~~
622 ~~which may also be related to the better performance of the MODIS DT algorithm in vegetation-~~
623 ~~covered regions. In high aerosol load areas affected by deserts, such as Africa and Asia, the AOD of~~
624 ~~visibility inversion needs to be improved.~~

625 3.3.3 Validation at a site scale

626 Sites, especially AERONET, are not completely uniform across the world or in any region, and
627 different stations have different sample sizes, which may lead to a certain uncertainty. Therefore,
628 further analysis was conducted on the spatial distribution of different evaluation metrics. Figure 87
629 shows the validation and comparison of daily VIS_AOD against Terra and AERONET AOD at a
630 site scale.

631 Compared to Terra daily AOD, the R of 67% stations is greater than 0.4, the mean bias of 83% is

Table 1: Evaluation metrics for the relationships between visibility-derived AOD and AERONET AOD and Terra AOD for each region.

Region		N			R			RMSE			MAE			Within EE (%)		
		daily	monthly	yearly	daily	monthly	yearly	daily	monthly	yearly	daily	monthly	yearly	daily	monthly	yearly
Eastern Europe	AERONET	21724	2317	271	0.463	0.493	0.653	0.1069	0.0647	0.0326	0.0714	0.0442	0.0263	65.69	83.77	97.42
	TERRA	661630	36435	3278	0.464	0.665	0.790	0.1095	0.0471	0.0214	0.0726	0.0286	0.0122	66.07	94.71	99.18
Western Europe	AERONET	53043	6033	697	0.445	0.487	0.344	0.1089	0.0716	0.0513	0.0711	0.0474	0.0347	64.40	79.21	89.10
	TERRA	1778013	104620	9166	0.467	0.763	0.811	0.1096	0.0391	0.0210	0.0712	0.0268	0.0124	66.99	95.42	99.40
Western North America	AERONET	33859	2948	334	0.503	0.484	0.509	0.1465	0.0949	0.0566	0.0747	0.0597	0.0419	63.58	67.37	81.14
	TERRA	1725226	82734	7201	0.542	0.765	0.906	0.1144	0.0465	0.0180	0.0671	0.0267	0.0125	69.48	94.42	99.61
Eastern North America	AERONET	47407	5359	608	0.527	0.526	0.559	0.1135	0.0824	0.0436	0.0657	0.0472	0.0331	67.52	77.78	87.50
	TERRA	6280277	359520	31343	0.515	0.799	0.847	0.1159	0.0435	0.0165	0.0726	0.0275	0.0111	66.70	94.94	99.80
Central South America	AERONET	10911	1176	149	0.740	0.811	0.866	0.1735	0.1272	0.1060	0.1021	0.0904	0.0688	52.40	47.96	67.79
	TERRA	444780	26362	2410	0.545	0.820	0.776	0.1447	0.0591	0.0369	0.0909	0.0396	0.0219	58.48	89.29	97.39
Southern Africa	AERONET	4255	309	38	0.423	0.480	0.630	0.1553	0.1128	0.0705	0.1033	0.0805	0.0525	52.08	59.55	78.95
	TERRA	216239	11304	1118	0.518	0.821	0.870	0.1258	0.0511	0.0296	0.0836	0.0340	0.0191	60.64	91.70	98.21
Australia	AERONET	6426	516	63	0.488	0.654	0.363	0.1094	0.0827	0.0725	0.0711	0.0620	0.0563	59.96	59.88	71.43
	TERRA	284693	14588	1286	0.398	0.784	0.831	0.1091	0.0363	0.0188	0.0666	0.0261	0.0143	67.01	94.65	99.38
Western Africa	AERONET	2205	205	34	0.553	0.594	0.762	0.3180	0.2873	0.3357	0.2082	0.2029	0.2587	37.96	40.00	23.53
	TERRA	156392	10468	1028	0.501	0.769	0.849	0.1769	0.0706	0.0412	0.1198	0.0482	0.0242	51.83	88.01	97.57
Southeast Asia	AERONET	4134	504	74	0.405	0.542	0.488	0.2037	0.1447	0.1198	0.1274	0.0988	0.0821	50.17	56.15	60.81
	TERRA	402465	27058	2500	0.470	0.753	0.872	0.1730	0.0729	0.0342	0.109	0.0455	0.0198	57.25	87.01	97.96
Eastern China	AERONET	7396	927	118	0.513	0.551	0.356	0.3571	0.2355	0.1933	0.2038	0.1392	0.1382	40.10	49.84	50.00
	TERRA	241185	17324	1518	0.523	0.811	0.895	0.1646	0.0638	0.0302	0.1073	0.0435	0.0225	55.77	88.07	98.88
Northeast Asia	AERONET	9979	1178	142	0.569	0.593	0.367	0.4941	0.3249	0.2604	0.2924	0.2425	0.2202	35.17	29.54	21.13
	TERRA	78823	5485	467	0.553	0.872	0.965	0.1973	0.0636	0.0263	0.1201	0.0440	0.0198	56.48	87.77	98.29

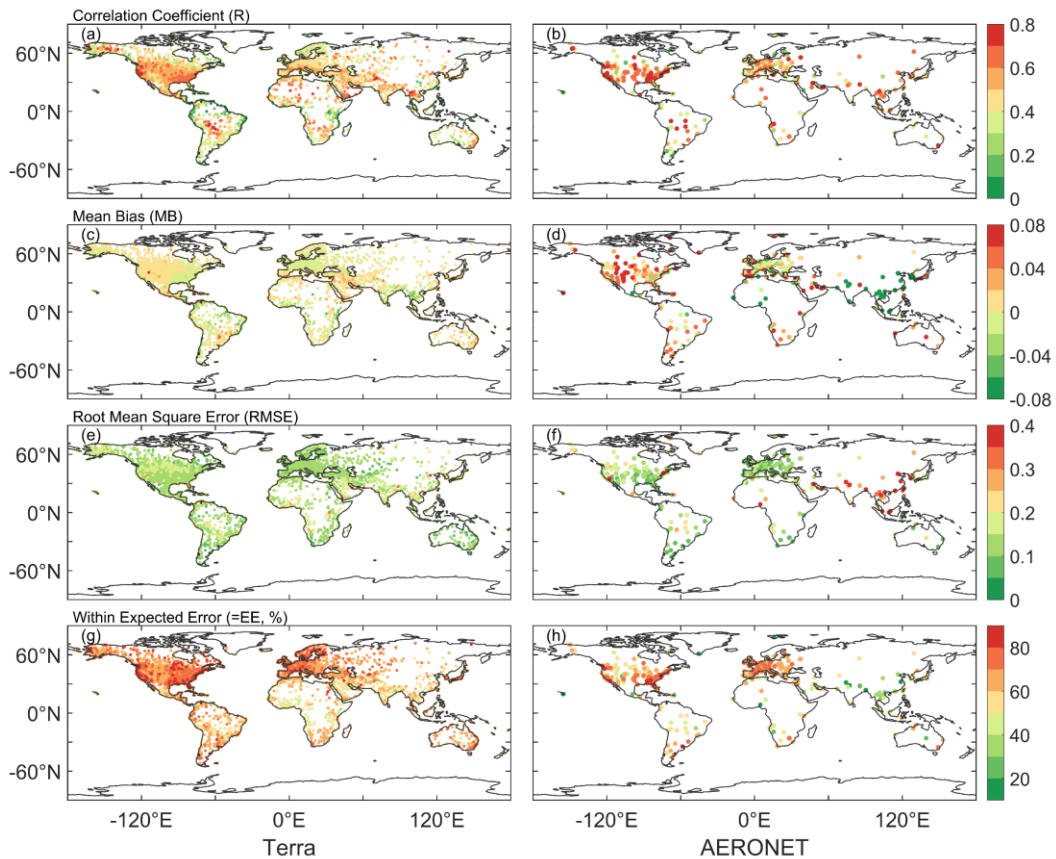
<i>India</i>	<i>AERONET</i>	2208	203	32	0.521	0.462	0.534	0.2957	0.3015	0.3588	0.2049	0.2283	0.2862	32.11	24.63	15.63
	<i>TERRA</i>	179928	9564	862	0.526	0.815	0.915	0.1564	0.0599	0.0352	0.1089	0.042	0.0238	55.16	90.43	98.14

633

634 less than 0.01, the RMSE of 85% is less than 0.15, and the percentage falling within the EE of 67%
635 is greater than 60%. More than 85% of stations fall within the EE is greater than 60% in Europe,
636 North America, and Oceania, while 40-60% in South America, Africa, and Asia. The percentage of
637 expected error is low in South and East Asia, and Central Africa, with some underestimation. Above
638 60% in Africa, Asia, North America, and Europe have a correlation coefficient greater than 0.4. The
639 regions with lower correlation are the coastal regions of South America, eastern Africa, western
640 Australia, northeastern North America, and northern Europe. Above 90% of the RMSE in Europe,
641 North America, and Oceania have a correlation coefficient smaller than 0.15. High RMSE regions
642 are in western North America, Asia, central South America, and central Africa.

643 Compared to AERONET daily AOD, the R of 74% stations is greater than 0.4, and the spatial
644 distribution is similar to Terra's. The mean bias of 44% is less than 0.01, the RMSE of 68% is less
645 than 0.15, and the percentage falling within the EE of 53% is greater than 60%. More than 70% of
646 sites have a correlation coefficient greater than 0.4 in Africa, Asia, Europe, and North America.
647 More than 57% of sites have an expected error percentage of over 60% in Europe, North America,
648 and Oceania, ~~e-~~ Except for Asia. Over 72% of sites have a RMSE less than 0.15. Except for Oceania
649 and South America, over 71% of sites in other regions have MAE less than 0.01. Almost all sites in
650 Asia show a negative bias, significantly underestimating. However, there is a significant
651 overestimation in western North America and western Australia. Most sites in Asia falling within
652 the expected error are less than 50%. High RMSE ~~region~~ are in high emission and dust areas, such
653 as Asia, India, and ~~central~~ Africa.

654
655 The validation and comparison on the site scale show a limitation similar to the MODIS ~~DT~~ ~~DT~~
656 algorithm. In areas with high vegetation coverage, the AOD from visibility are better than those in
657 bright areas ~~such as deserts~~. Although the correlation coefficients are high in high aerosol loading
658 areas (Central South America, West Africa, India, Eastern China, Northeast Asia), there are
659 significant differences in these areas with high RMSE values. As shown in Figure 6, some stations
660 located in dusty and urban areas are overestimated or underestimated. Studies have shown that there
661 is significant uncertainty in the MODIS retrievals in these regions, and the challenges of inversion
662 algorithms are significant in bright surfaces (desert and snow covered areas) and urban surface of
663 densely populated complex structures (Chu et al., 2002; Remer et al., 2005; Levy et al., 2010; Wei
664 et al., 2019; Wei et al., 2020). In India, the elevation difference between AERONET site and
665 meteorological station reached 0.7km may be a factor affecting the validation effect, as aerosol
666 varies greatly with altitude. In eastern China, the complex urban surface, emission sources, and
667 observations in different locations (AERONET site and meteorological station) may be the reasons
668 for underestimation. At the same time, visibility stations in desert areas are sparse, and the spatial
669 variability of dust aerosols is large, which also increases the difficulty to estimate VIS_AOD.



670
 671 **Figure 8:7** Validation of VIS_AOD against Terra and AERONET AODs at each site: (a–b)
 672 correlation (R), (c–d) mean bias (MB), (e–f) root mean square error (RMSE), (g–h) percentage (%)
 673 of VIS_AOD within the expected error envelopes.

674 3.3.4 Discussion and uncertainty analysis

675 The atmospheric visibility is a horizontal physical quantity, while AOD is a column-integrated
 676 physical quantity. We have linked the two variables together using machine [a](#) learning methods,
 677 which partially compensates for the scarcity of AOD data. However, we have to face some
 678 limitations. Although the boundary layer height is considered, it is not sufficient. Pollutants such as
 679 smoke from biomass burning, dust, volcanic ash, and gas-aerosol conversion of sulfur dioxide to
 680 sulfate aerosols in the upper and lower troposphere can undergo long-range aerosol transport under
 681 the influence of circulation. The pollution transport and aerosol conversion processes above the
 682 boundary layer are still significant and cannot be ignored (Eck et al., 2023). Compared to surface
 683 visibility, bias occurs when the aerosol layer rises and affects AERONET measurements and
 684 MODIS retrievals. Therefore, it should be considered when using this data. If there were sufficient
 685 historical vertical aerosol measurements with high temporal and spatial resolution, the results of this
 686 data would be greatly improved. Although some studies use aerosol profiles from pollution transport
 687 models or assumed profiles as substitutes for observed profiles (Li et al., 2020; Zhang et al., 2020),
 688 the biases introduced by these non-observed profiles are still significant.

689 In machine learning, we used MODIS Aqua AOD as the target value for the model because the
 690 validation results for MODIS C6.1 ~~products~~product have a correlation coefficient of 0.9 or higher
 691 with AERONET AOD ~~on~~at the daily scale (Wei et al., 2019; Wei et al., 2020). Compared to
 692 AERONET, MODIS AOD provides more sample data with a high global coverage. However, apart

693 from modeling errors, the systematic biases and uncertainties of MODIS Aqua AOD cannot be
694 ignored (Levy et al., 2013; Levy et al., 2018; Wei et al., 2019). Averaging over time scale can reduce
695 representation errors effectively, and emission sources and orography can increase representation
696 errors~~Averaging over time scale significantly reduces systematic errors but cannot diminish errors~~
697 ~~caused by emission sources and terrain. Therefore, the strong correlation at monthly and annual~~
698 ~~scales indicates a substantial reduction in errors~~ (Schutgens et al., 2017). Therefore, the strong
699 correlation at monthly and annual scales indicates a substantial reduction in errors. This is also one
700 of the reasons why this dataset shows stronger correlation with Terra AOD and weaker correlation
701 with AERONET in validation.

702 The spatial matching between meteorological stations and AERONET sites may cause some biases.
703 AERONET sites are usually not co-located with meteorological stations in terms of elevation and
704 horizontal distance, this is another reason for the weak correlation between VIS_AOD and
705 AERONET AOD. The meteorological stations are located at the airport. Different horizontal
706 distances may result in meteorological stations and AERONET sites being located on different
707 surfaces (such as urban, forest, mountainous). Differences in site elevation significantly impact the
708 relationship between AOD and measured visibility. When the AERONET site is at a higher elevation
709 than the meteorological station, there may be fewer measurements of aerosols over the sea at the
710 AERONET site.

711 Different pollution levels and station elevation affect the AOD derived from visibility. The elevation
712 difference and distance between meteorological stations and AERONET sites also have an impact
713 on the validation results. Therefore, the error and performance of different AERONET AOD values,
714 station elevation, and distance ~~were~~are analyzed.

715 **~~3.3.4.1 Uncertainty with pollution level~~**

716 As the AOD increases, the variability of bias also increases in Figure 98 (a). Almost all mean bias
717 values are within the envelope of EE, except for 1.1-1.2 and 1.5-1.6. The average bias is 0.015
718 (AOD <0.1), with 83% of data within the EE envelopes. The mean bias is -0.0011 (AOD, 0.1-0.2),
719 with 54% within the EE envelopes. The mean bias is negative (AOD, 0.3-1.0), with 20%-40%
720 falling within the EE envelopes. There is a positive bias (AOD, 1.1, 1.4 and >1.6), and there is a
721 negative bias at 1.2-1.3 and 1.5-1.6. The results indicate that as pollution level increases, the
722 negative mean bias becomes significant and the underestimation increases.

723 **~~3.3.4.2 Uncertainty with elevation of AERONET site~~**

724 The contribution of particulate matter near the ground to the column aerosol loading is significant.
725 The elevation of the site affects the measurement of column aerosol loading in Figure 8-9 (b). There
726 is a negative bias in the low elevation (≤ 0.5 km) with a percentage of 60%-64% falling within the
727 EE envelopes and a positive bias in high elevation (0.5-1.2km) with a percentage of 50%-65%
728 falling within the EE envelopes. The percentage significantly decreases (> 1.2 km), and the average
729 bias increases. Therefore, the elevation of AERONET's site will cause bias in validation, and the
730 uncertainty greatly increases in high elevation.

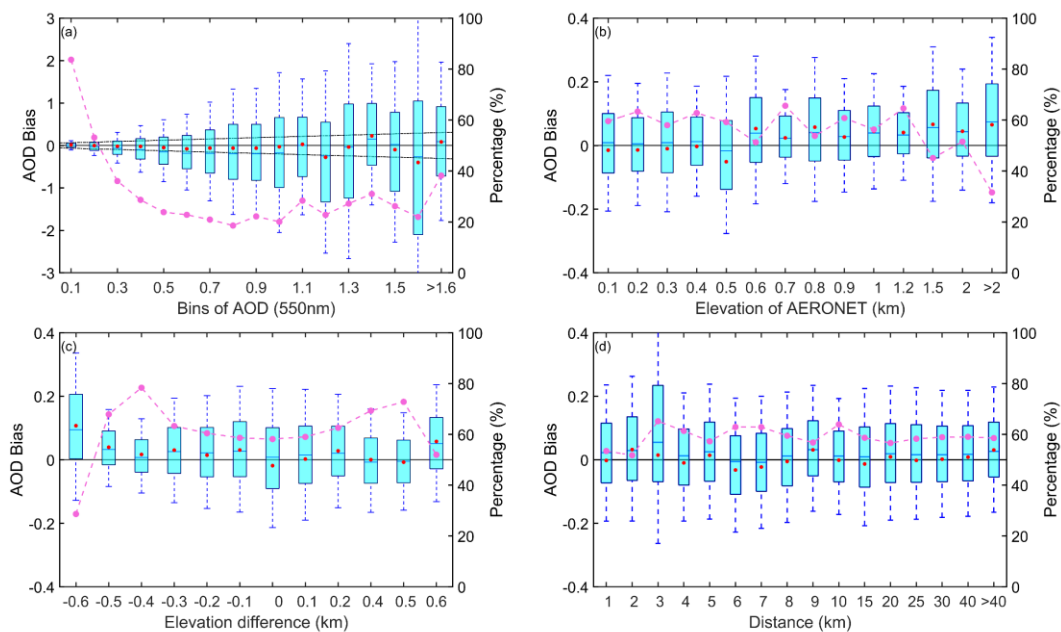
731 **~~3.3.4.3 Uncertainty with elevation of meteorological station~~**

732 Due to the elevation difference between the meteorological station and AERONET site in the
733 vertical direction, the uncertainty caused by elevation differences of site was analyzed in Figure 8-9

734 (c). When the elevation difference is negative (the elevation of the meteorological station is lower
 735 than that of the AERONET station), there is a significant positive bias. When the difference is
 736 positive, the mean bias approaches 0 or is positive. The percentage is greater than 60% (-0.5 km-
 737 0.5km). The positive mean bias is greater than the negative mean bias, and the uncertainty greatly
 738 increases when the elevation of meteorological stations is lower than that of AERONET sites. It
 739 indicates that the contribution of the near surface aerosol to the column aerosol loading is significant
 740 and cannot be ignored.

741 **3.3.4.4 Uncertainty with distance between meteorological station and AERONET site**

742 The spatial variability of aerosols is significant. Meteorological stations and AERONET sites are
 743 not collocated, resulting in a certain distance in spatial matching. In this study, the upper limit of
 744 distance is 0.5 degree. Figure 8-9 (d) shows the error of the distance between stations, where the
 745 degree is converted to the distance at WGS84 coordinates. The bias does not change significantly
 746 with increasing distance. The average bias is around 0, with the maximum positive mean bias
 747 (0.0322) at a distance of 2km and the maximum negative mean deviation (-0.0323) at 6km. The
 748 median is almost positive, except at 5km and 6km. The percentage falling within the EE envelopes
 749 is over 50%, with the maximum percentage (66%) at 3km and the minimum (62%) at 2km.
 750



751

752 **Figure 89:** Box plots of AOD bias and the percentage falling within the EE envelopes (curves): (a)
 753 AERONET AOD levels, (b) elevation of AERONET sites, (c) elevation difference between
 754 meteorological stations and AERONET sites, (d) distance (km) between meteorological stations and
 755 AERONET sites. The black horizontal line represents the zero bias. For each box, the upper, lower,
 756 and middle horizontal lines, and whiskers represent the AOD bias 75th and 25th percentiles, median,
 757 and 1.5 times the interquartile difference, respectively. The black solid lines represent the EE
 758 envelopes ($\pm(0.05+0.15*AOD_{AERONET})$). No site with a difference of +0.3km (x-axis label without
 759 0.3) in (c).

3.4 Gridded visibility-derived AOD

3.4.1 Uncertainty of gridded AOD

We calculate the width of the 95% CI for gridded AOD. Figure 10 (a-b) shows the spatial distribution and frequency of the 95% CI from 1980 to 2021. In areas with dense visibility stations, the kriging variance is low, the width of 95% CI is small, and the uncertainty of the gridded AOD is low. In areas with sparse visibility stations, the width is large, and the uncertainty is high. The uncertainty of approximately 43% of the grids is less than 0.03, and nearly 80% has an uncertainty less than 0.06. Approximately 7% of the grids have an uncertainty larger than 0.1. Regions with low uncertainty are mainly located in North America (<60°N), Europe, Western and Southern Asia, Eastern China, and South America. Regions with high uncertainty are found in high-latitude areas (e.g., Siberia), high-altitude regions (e.g., Tibetan Plateau), and desert areas (such as the Sahara Desert, Taklamakan Desert, and Australian deserts).

Uncertainty also exhibits seasonal variations, as shown in Figures (c-f). The percentage of grid cells with uncertainty less than 0.06 is 63%, 84%, 77%, and 86% in DJF, MAM, JJA, and SON, respectively. Compared to other seasons, uncertainty increases significantly in high-latitude regions, Africa, northern Asia, Oceania, and eastern South America during DJF. In JJA, the distribution of uncertainty is similar to DJF, but the uncertainty decreases. In MAM and JJA, there is higher confidence, with a small number of grid cells having large uncertainty (>0.1), primarily concentrated in high-latitude regions.

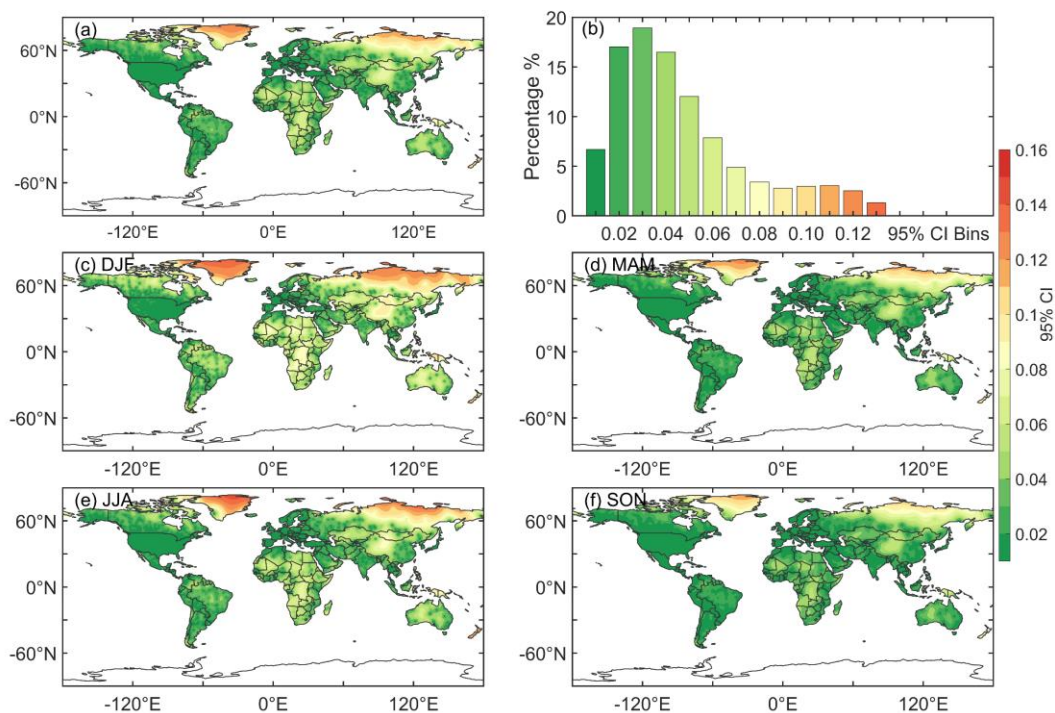


Figure 10: The spatial distribution (a) and frequency (b) of the 95% confidence interval (CI) from 1980 to 2021. The spatial distribution of the width of the 95% CI for each season (c-f). Bins of 95% CI are from 0 to 0.15 with an interval of 0.01. DJF represents December and next January and February. MAM represents March, April, and May. JJA represents June, July, and August. SON represents September, October, and November.

3.4.2 Comparison with Aqua/Terra MODIS AOD

Figure 119 shows the gridded AOD based on ordinary kriging interpolation with the area-weighted method and compares the multi-year spatial, zonal, and meridional distributions of AOD with Aqua and Terra AOD over land from 2003 to 2021. The VIS_AOD is 0.157 ± 0.073 over land, which is almost equal to the Aqua (0.152 ± 0.084) and Terra (0.154 ± 0.088) AOD values with relative biases of 3.3%, and 1.9%, respectively. In order to compare the spatial correlation, Aqua and Terra MODIS AOD are averaged to the 0.5-degree resolution. In the heatmap (Figure 120), the R of VIS_AOD and Aqua AOD is 0.798, the RMSE is 0.049 with a bias of 32% compared to the mean, and the MAE is 0.008, with a bias of 5% compared to the mean. Compared to Terra AOD, the R is 0.787, and the RMSE is 0.051, with a bias of 33% compared to the mean, and the MAE is 0.005, with a bias of 3% compared to the mean. The R between Aqua and Terra AOD is 0.980. The R values between VIS_AOD and Aqua and Terra AOD are 0.995 and 0.990 for the zonal distribution and 0.986 and 0.897 for the meridional distribution, respectively. In the low aerosol loading region, VIS_AOD exhibits a little overestimation. Whether in meridional or zonal distribution, the peak and valley regions are basically consistent (Tian et al., 2023). Due to the limitations of satellite inversion algorithms, a bias appears on the bright surface, especially in northern North America with extensive snow cover (Levy et al., 2013). All above results suggest that the gridded AOD is consistent with satellite retrievals observations in spatial distribution.

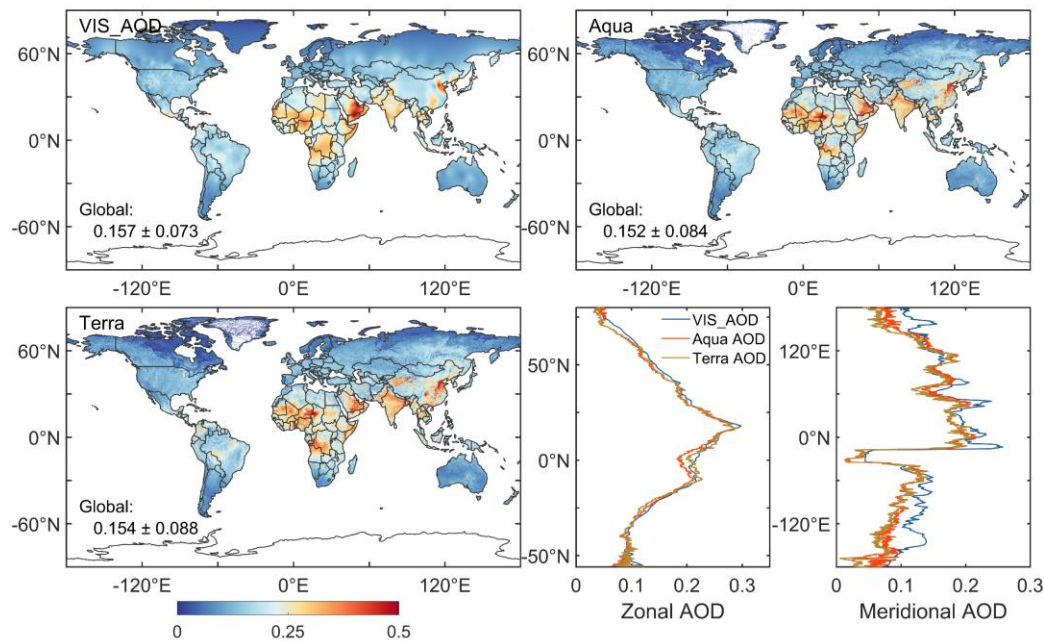
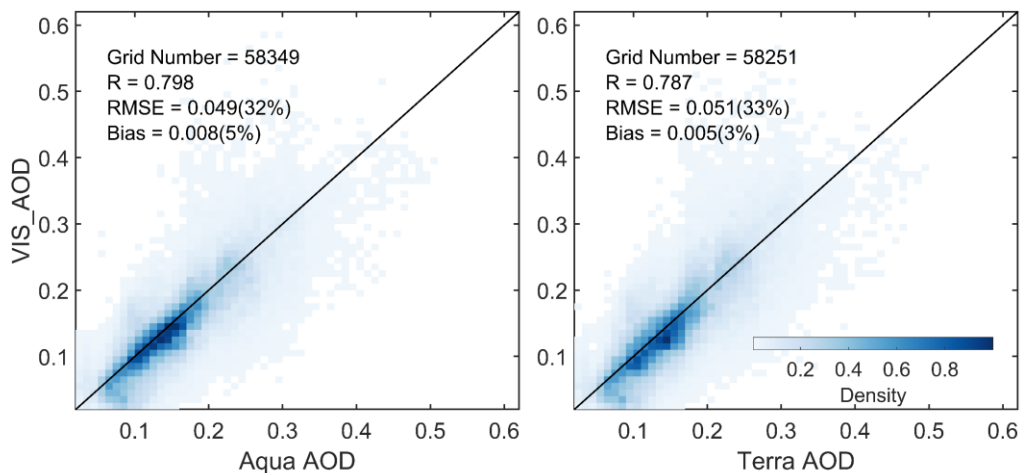


Figure 9-11: The spatial, zonal and meridional distributions of the multi-year mean VIS_AOD, Aqua AOD, and Terra AOD over land from 2003 to 2021.



808

809 **Figure 12:0** Heatmap of multi-year mean gridded VIS_AOD and Aqua AOD and Terra AOD during
 810 2003-2021. Terra and Aqua AOD are averaged onto a grid of 0.5°.

811 3.5 Interannual variability and trend of visibility-derived AOD over global land

812 The spatial distribution of multi-year average AOD from 1980 to 2021 over land is shown in Figure
 813 134 (a). The mean AOD of land (-60-85°N), Northern Hemisphere (NH, 0-85°N), and the Southern
 814 Hemispheres (SH, -60-0°N) is 0.161 ± 0.074 , 0.158 ± 0.076 , and 0.173 ± 0.059 , respectively. The
 815 AOD values of Africa, Asia, Europe, North America, Oceania, and South America are 0.241, 0.222,
 816 0.110, 0.111, 0.129 and 0.117, respectively.

817 Due to the influence of geography, atmospheric circulation, population, and emissions, the AOD
 818 varies in different latitudes. Figure 12-14 illustrates the multi-year average AOD in different latitude
 819 ranges for land, the NH, and the SH from 1980 to 2021. Within [-20, 20°N], the global average AOD
 820 reaches its maximum (0.234), and the maximum AOD NH is 0.256 in [0, 20°N]. The highest AOD
 821 in SH is 0.217 in [-15, 0°N]. The average AOD in SH rapidly decreases from -15°N to -35°N. In
 822 NH, AOD is generally greater than in SH from 5°N to 65°N. When, the latitude is greater than 70°N,
 823 the NH's AOD is smaller than the SH's.

824 There are many regions of high AOD values occur in NH, with the distribution of population density.
 825 Approximately 7/8 of the global population resides in the NH, with 50% concentrated at 20°N-40°N
 826 (Kummu et al., 2016), indicating a significant impact of human activities on aerosols. The highest
 827 AOD values are observed near 17°N, including the Sahara Desert, Arabian Peninsula, and
 828 southeastern India, suggesting that in addition to anthropogenic sources, deserts also play a crucial
 829 role in aerosol emissions. Lower AOD regions of the SH are from 25°S to 60°S, encompassing
 830 Australia, southern Africa, and southern South America, indicating lower aerosol burdens in these
 831 areas. Additionally, North America also exhibits low aerosol loading. Chin et al. (2014) analyzed
 832 the AOD over land from 1980 to 2009 with the Goddard Chemistry Aerosol Radiation and Transport
 833 model, which is similar to the visibility-derived AOD. The spatial distribution is consistent with the
 834 satellite results (Remer et al., 2008; Hsu et al., 2012; Hsu et al., 2017; Tian et al., 2023). The AOD
 835 and extinction coefficient retrieved from visibility show a similar distribution at global scale, with
 836 a correlation coefficient of nearly 0.6 (Mahowald et al., 2007). Similar global (Husar et al., 2000;
 837 Wang et al., 2009) and regional (Koelemeijer et al., 2006; Wu et al., 2014; Boers et al., 2015; Zhang

838 et al., 2017; Zhang et al., 2020) spatial distributions have been reported.

839 AOD loadings exhibit significant seasonal variations worldwide, particularly over land. In this study,
840 a year is divided into four parts: December-January-February (DJF), March-April-May (MAM),
841 June-July-August (JJA), and September-October-November (SON), corresponding to winter
842 (summer), spring (autumn), summer (winter), and autumn (spring) in NH (SH), respectively. Figure
843 134 (b-e) also depicts the spatial distribution of seasonal average AOD over land from 1980 to 2021.
844 The global AOD in DJF, MAM, JJA, and SON is 0.158 ± 0.062 , 0.162 ± 0.081 , 0.175 ± 0.093 , and
845 0.153 ± 0.070 , respectively. The standard bias of AOD in JJA and MAM are greater than those in
846 DJF and SON. AOD exhibits seasonal changes, with the highest in JJA, followed by MAM, DJF,
847 and SON. From 1980 to 2021, the seasonal AOD in NH is 0.152 ± 0.064 (DJF), 0.161 ± 0.088 (MAM),
848 0.176 ± 0.090 (JJA), and 0.144 ± 0.060 (SON), and in SH is 0.184 ± 0.041 (DJF), 0.166 ± 0.044 (MAM),
849 0.169 ± 0.072 (JJA), and 0.19 ± 0.060 (SON).

850 In NH, the AOD ranking from high to low in season is summer > spring > winter > autumn. In SH,
851 the AOD ranking from high to low in season is spring > summer > winter > autumn. The highest
852 AOD is observed during JJA in NH, while in SH, the peak occurs during SON. The occurrence of
853 high AOD values is highly associated with the growth of hygroscopic particle and the photochemical
854 reaction of aerosol precursors under higher relative humidity in Asia (JJA) (Remer et al., 2008) and
855 Europe such as Russia (JJA), and biomass burning in South America (SON), Southern Africa (SON),
856 and Indonesia (SON) (Ivanova et al., 2010; Krylov et al., 2014). On the other hand, the lowest global
857 AOD values are observed during autumn, which may be attributed to the weakening of monsoon
858 systems (Li et al., 2016; Zhao et al., 2019).

859 In addition to the spatial characteristics of AOD, the temporal variations in AOD have also been of
860 great interest due to the significant relationship between aerosols and climate change. Figure 134 (f)
861 shows the temporal trends of annual average AOD (** represents passing the significance test,
862 $p<0.01$) over the global land, the SH and the NH during 1980-2021. The global land, NH, and SH
863 trends demonstrate decreasing trends of AOD with values of $-0.0026/10a$, $-0.0018/10a$, and $-$
864 $0.0059/10a$, respectively, with all passing the significance test with a confidence level of 95%.
865 Notably, the declining trend is much greater in the SH than in the NH. It may be related to the
866 decrease in the frequency of sandstorms and wildfires and the increase in precipitation, such as in
867 Australia. Two AOD peaks in 1983 and 1994 and two AOD valleys in 1980 and 1990 are observed
868 before 2000. The two AOD peaks may be attributed to large volcanic eruptions, which has been
869 confirmed by previous studies. The volcanic eruptions and their associated fires of the El Chichón
870 volcano in Mexico in 1982 (Hirono and Shibata, 1983) and Mount Pinatubo in the Philippines in
871 1991 (Tupper et al., 2005) resulted in elevating global AOD levels in the following years. The AOD
872 recovery to the previous low levels after volcanic eruptions takes approximately 10 years (Chazette
873 et al., 1995; Sun et al., 2019). This further indicates the efficiency of our data capturing the volcanic
874 eruption emission features.

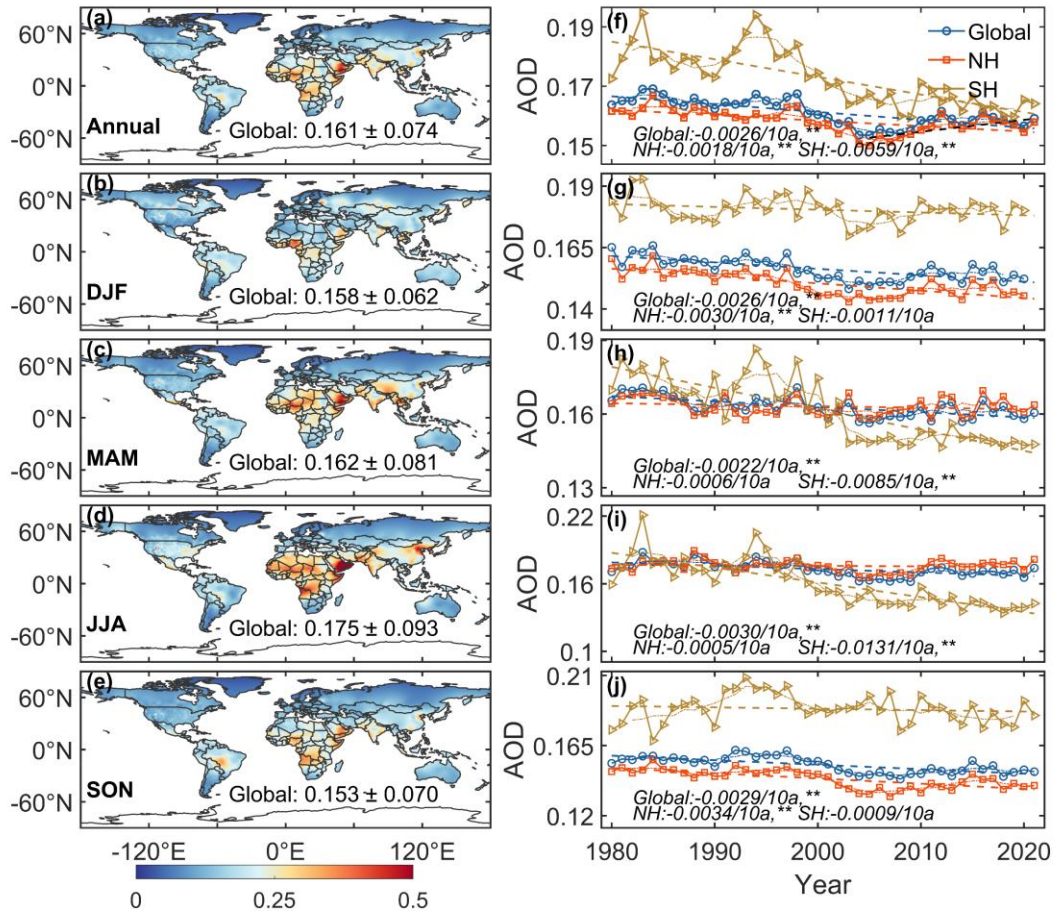
875 Due to the influence of geography, atmospheric circulation, population, and emissions, the trend of
876 global aerosols varies in different latitude Figure 12-14 illustrates the multi-year average AOD in
877 different latitude ranges for land, the NH, and the SH from 1980 to 2021. Within $[-20, 20^{\circ}N]$, the
878 global average AOD reaches its maximum (0.234), and the maximum AOD NH is 0.256 in $[0, 20^{\circ}N]$.
879 The highest AOD in SH is 0.217 in $[-15, 0^{\circ}N]$. The average AOD in SH rapidly decreases from -

880 15°N to -35°N. In NH, AOD is generally greater than in SH from 5°N to 65°N. When, the latitude
881 is greater than 70°N, the NH's AOD is smaller than the SH's, which may be related to low emission
882 intensity and low population density in high latitude areas.

883 The seasonal trends of AOD during 1980-2021 at the global and hemispheric scales are shown in
884 Figure 134 (g-j). The global AOD shows a decreasing trend in all seasons (-0.002~-0.003/10a). The
885 large declining trends are observed in JJA and SON, with decreasing trend values of -0.003/10a and
886 -0.0029/10a, respectively. DJF and MAM follow with decreasing trend values of -0.0026/10a and -
887 0.0022/10a, respectively, all passing the significance test ($p < 0.01$). For the NH, the AOD trends in
888 different seasons are -0.0030/10a (DJF), -0.0006/10a (MAM), -0.0005/10a (JJA), and -0.0034/10a
889 (SON). DJF and SON pass the significance test ($p < 0.01$), while MAM and JJA do not. In the SH,
890 the trends are as follows: -0.0011/10a (DJF), -0.0085/10a (MAM), -0.0131/10a (JJA), and -
891 0.0009/10a (SON). Interestingly, in contrast to the NH, MAM and JJA pass the significance test,
892 while DJF and SON do not. The largest declining season in the NH is winter, while in the SH, it is
893 summer. The decreasing trend in the SH is more than four times greater than that in the NH,
894 particularly before the year 2000. While both the global and SH AOD exhibit a decreasing trend
895 since 2005, the NH has shown a significant increase in winter AOD, leading to an overall increasing
896 trend. Moreover, the NH shows an increasing trend of 0.004/10a from 2005 to 2021.

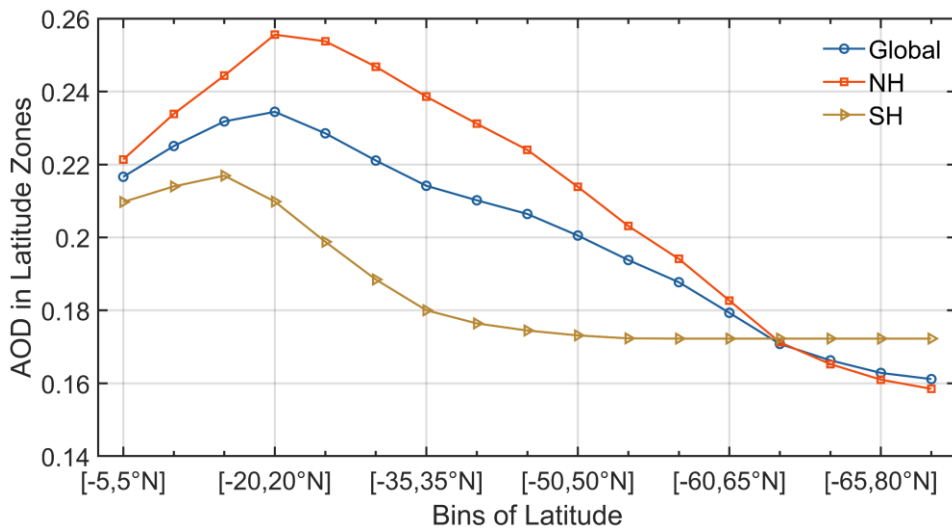
897 Annual SO₂ emissions increased from 9.4 to 15.3 TgS from 2000 to 2005, which ultimately ended
898 up as sulfate aerosols, leading to a significant increase in sulfate aerosols (Hofmann et al., 2009).
899 More relevantly, the frequent volcanic eruptions in tropical regions from 2002 to 2006, combined
900 with seasonal circulation patterns during winter, led to the transport of aerosol particles to higher
901 latitudes (Hofmann et al., 2009; Vernier et al., 2011; Sawamura et al., 2012; Andersson et al., 2015).

902



903

904 **Figure 13:1** The multi-year averages of VIS_AOD from 1980 to 2021. Global land (circle), northern
 905 hemisphere (NH, 0-85°N) (triangle) and southern hemisphere (SH, 0-60°S) (square) annual and
 906 seasonal AOD. The symbol, **, represents that the test passed at a significance level of 0.01. DJF
 907 represents December and next January and February. MAM represents March, April, and May. JJA
 908 represents June, July, and August. SON represents September, October, and November.



909

910 **Figure 14:2** The global land (blue), northern hemisphere's (red) and southern hemisphere's (yellow)

911 multi-year average VIS_AOD from 1980 to 2021 in different latitude zones. The latitude range is
912 from -60 to 85°N, with a bin of 5°.

913 **3.6 Interannual variability and trend of visibility-derived AOD over regions**

914 The distribution of AOD over global land exhibits significant spatial heterogeneity. Large variations
915 in aerosol concentrations exist among different regions, leading to a non-uniform spatial distribution
916 of AOD globally. Accurately assessing the long-term trends of aerosol loading is a key for
917 quantifying aerosol climate change, and it is crucial for evaluating the effectiveness of measures
918 implemented to improve regional air quality and reduce anthropogenic aerosol emissions.

919 To analyze the spatiotemporal characteristics and trends of AOD in different regions, we selected
920 12 representative regions that are influenced by various aerosol sources(Wang et al., 2009; Hsu et
921 al., 2012; Chin et al., 2014), such as desert, industry, anthropogenic emissions, and biomass burning
922 emissions, which nearly cover the most land and are densely populated regions (Kummu et al.,
923 2016). These representative regions are Eastern Europe, Western Europe, Western North America,
924 Eastern North America, Central South America, Western Africa, Southern Africa, Australia,
925 Southeast Asia, Northeast Asia, Eastern China, and India, as shown in Figure 1. We use multi-year
926 average and seasonal average AOD to evaluate aerosol loadings (Figure 1315), the annual average
927 of monthly anomalies to analyze interannual trends (Figure 1416), and the seasonal average to
928 analyze seasonal trends (Figure 1517) in 12 regions from 1980 to 2021.-

929 We can see some differences between VIS_AOD and MODIS AOD. In addition to model errors,
930 the spatial matching between meteorological stations and MODIS, terrain, surface coverage, and
931 station altitude will also bring errors. When particle transport and photochemical reactions occur
932 above the boundary layer, visibility cannot capture the feature, which will also increase the
933 uncertainty. However, bias is inevitable and can only be kept as small as possible. From the trend,
934 they have similar changing characteristics, especially on monthly and yearly scales.-

935 Figure 13-15 shows the regions with high AOD level from 1980 to 2021 (multi-year average AOD >
936 0.2) are in West Africa, Northeast Asia, Eastern China, and India. The AOD values in Eastern North
937 America, Central South America, South Africa, and Southeast Asia range from 0.15 to 0.2. The
938 AOD values in Eastern Europe, Western Europe, Western North America, and Australia are less than
939 0.15.-

940 Europe is an industrial region with a low aerosol loading region, and the multi-year average AOD
941 in Eastern Europe (0.144 ± 0.007) is higher than that in Western Europe (0.139 ± 0.003) during 1980-
942 2021. Eastern Europe shows a greater downward trend in AOD ($-0.0041/10a$) compared to Western
943 Europe ($-0.0021/10a$). The highest AOD is observed in JJA, the dry period when solar irradiation
944 and boundary layer height increase, with Eastern Europe at 0.161 and Western Europe at 0.162,
945 which could be due to increases in secondary aerosols, biomass burning, and dust transport from
946 the Sahara (Mehta et al., 2016). However, there are seasonal variations. In Eastern Europe, the
947 seasonal AOD ranking from high to low is JJA (0.161) > DJF (0.147) > MAM (0.138) > SON
948 (0.131), while in Western Europe, it is JJA (0.162) > MAM (0.140) > SON (0.136) > DJF (0.117).
949 The differences among seasons are larger in Western Europe. AOD in Eastern Europe shows
950 declining trends in all seasons, while it does not pass the significance test in MAM. Among four
951 seasons, SON has the largest decline trend of AOD ($-0.0058/10a$). In Western Europe, DJF, JJA, and

952 SON exhibit declining trends of AOD that pass the significance test, while the MAM shows a
953 significant increase trend of AOD (0.0022/10a), which may be due to eruptions of the
954 Eyjafjallajökull volcano in Iceland in spring 2010 (Karbowska and Zembrzuski, 2016). Both
955 Western and Eastern Europe experienced increasing trends in AOD during the period of 1995-2005,
956 with Western Europe showing a greater increase. However, after 2000, the decline rate accelerated
957 in both regions. The downward trend in Europe is attributed to the reduction of biomass burning,
958 anthropogenic aerosols, and aerosol precursors (such as sulfur dioxide)(Wang et al., 2009; Chin et
959 al., 2014; Mortier et al., 2020).

960 North America is also an industrial region with a low aerosol loading. The average AOD values for
961 Eastern and Western North America during 1980-2021 are 0.153 ± 0.004 and 0.131 ± 0.005 ,
962 respectively, with the Eastern region being higher than the Western region by 0.022. From 1980 to
963 2021, both Eastern (-0.0021/10a) and Western North America (-0.0009/10a) show a downward trend;
964 however, the decline in the Western region is not statistically significant. And the trend is -
965 0.0172/10a from 1995 to 2005 and 0.0096/10a from 2005 to 2021. The average AOD values in DJF,
966 MAM, JJA, and SON in Western North America are 0.1367, 0.1286, 0.1457, and 0.114, respectively,
967 compared to 0.137, 0.145, 0.1913, and 0.138 in Eastern North America. The lowest AOD values of
968 12 regions during DJF and SON are observed in Western North America (Remer et al., 2008).
969 Specifically, in the Western region, there is a consistent increasing trend during MAM (0.004/10a)
970 from 1980 to 2021, while JJA and SON also show an increase after 2000, except for DJF (-
971 0.0032/10a). In contrast, the AOD trends in the Eastern region remain unchanged during the period
972 1980-2021, except for MAM, which shows a stable increasing trend (0.0033/10a), while DJF, JJA,
973 and SON exhibit decreasing trends (-0.0023/10a, -0.0040/10a, -0.0053/10a, respectively). In the
974 Western region, the annual mean AOD started to increase after 2005, while in the Eastern region,
975 the increase was not significant. The upward trend may be due to low rainfall and increased wildfire
976 activities (Yoon et al., 2014). The decrease in AOD in Eastern North America is related to the
977 reduction of sulfate and organic aerosols, as well as the decrease in anthropogenic emissions caused
978 by environmental regulations (Mehta et al., 2016).

979 Central South America is a relatively high aerosol loading region, sourced from biomass burning,
980 especially in SON (Remer et al., 2008; Mehta et al., 2016), with a multi-year average AOD of
981 0.192 ± 0.017 . There is a clear downward trend (-0.0100/10a) from 1980 to 2021, which is slightly
982 greater than the trend (-0.0090/10a) from 1998 to 2010 (Hsu et al., 2012) and AOD decreased from
983 1980 to 2006 (Streets et al., 2009) and from 2001 to 2014 (Mehta et al., 2016). Although DJF (0.199)
984 and SON (0.226) have higher values compared to MAM (0.180) and JJA (0.163), the large declining
985 trends are observed in MAM (-0.0126/10a) and JJA (-0.0167/10a). It indicates that although AOD
986 has decreased overall, the aerosol loading caused by seasonal deforestation and biomass combustion
987 is still large (Mehta et al., 2016).

988 Africa is also one of the regions with a high aerosol loading worldwide. In West Africa, the average
989 AOD is 0.275 ± 0.012 during 1980-2021, and the annual AOD shows a downward trend (-0.0008/10a,
990 $p>0.05$). The world's largest desert (Sahara Desert) is in West Africa, with much dust aerosol
991 discharged. AOD values in all seasons are above 0.25, with JJA (0.301) and MAM (0.300) reaching
992 0.3, and DJF and SON being 0.252 and 0.250, respectively. The AOD in DJF (-0.0135/10a, $p<0.01$)
993 and SON (-0.0026/10, $p>0.05$) exhibit decreasing trends, while JJA (0.0088/10a, $p<0.01$) and MAM
994 (0.0037/10a, $p>0.05$) show an opposite trend. The multi-year average AOD in South Africa is

995 0.177±0.020, lower than that of West Africa. The annual mean AOD in South Africa shows a
996 significant decrease (-0.0096/10a). The AOD values range from 0.12 to 0.2 during 2000-2009,
997 dominated by fine particle matter from industrial pollution from biomass and fossil fuel combustion
998 (Hersey et al., 2015). The average AOD values in DJF, MAM, JJA, and SON are 0.189, 0.162, 0.147,
999 and 0.210, respectively. JJA (-0.0268/10a, p<0.01), MAM (-0.0126/10a, p<0.01) and SON (-
1000 0.0001/10a, p>0.05) exhibit a downward AOD trend, while DJF (0.0006/10a, p>0.05) shows an
1001 upward trend. AERONET and simulation results also show a decreasing trend of AOD (Chin et al.,
1002 2014).

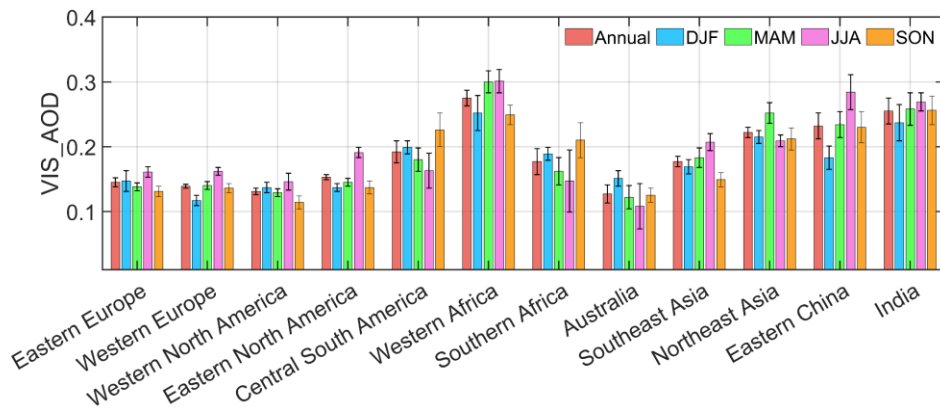
1003 Australia is a region with a low aerosol loading. The multi-year mean AOD is 0.127±0.014 during
1004 1980-2021. The AOD ranges from 0.05 to 0.15 from AERONET during 2000-2021, and dust and
1005 biomass burning are important contributors to the aerosol loading (Yang et al., 2021a). There is a
1006 downward trend of AOD (-0.0081/10a, p<0.01), which may be related to a decrease in dust and
1007 biomass burning (Yoon et al., 2016; Yang et al., 2021a). In addition, research has shown that the
1008 forest area in Australia has increased sharply since 2000 (Giglio et al., 2013), surpassing the forest
1009 fire area of the past 14 years. The seasonal average of AOD in MAM, JJA, SON, and DJF are 0.122,
1010 0.108, 0.125, and 0.151. The AOD in JJA is the lowest among all seasons and regions. The highest
1011 AOD is in DJF with an increasing trend (0.0056/10a, p<0.01), while the trends during MAM, JJA
1012 and SON are -0.0096/10a (p<0.01), -0.0231/10a (p<0.01) and -0.0042/10a (p<0.01), respectively.
1013 Ground-based observations and satellite observationsretrievals indicate that wildfires, biomass
1014 burning and sandstorms lead to high AOD in DJF and SON. The low AOD of MAM and JJA is due
1015 to a decrease in the frequency of sandstorms and wildfires and an increase in precipitation (Gras et
1016 al., 1999; Yang et al., 2021a; Yang et al., 2021b).

1017 Asia is also a high aerosol loading area with various sources. In Southeast Asia, the multi-year
1018 average AOD is 0.177 during 1980-2021 with a downward trend of AOD (-0.0003/10a, p>0.05). It
1019 is also a biomass-burning area. The seasonal average AOD ranking from high to low is JJA (0.207) >
1020 MAM (0.183) > DJF (0.169) > SON (0.149). The trends in DJF (-0.0035/10a, p<0.05), JJA (-
1021 0.0007/10a, p>0.05) and SON (-0.0021/10a, p>0.05) are opposite to MAM (0.0050/10a, p<0.01).
1022 Southeast Asia has no clear long-term trend in estimated AOD or observed surface solar radiation
1023 (Streets et al., 2009). In Northeast Asia, the multi-year average AOD is 0.222 during 1980-2021,
1024 with no significant temporal trend. The seasonal AOD values are 0.252 in MAM, 0.215 in DJF,
1025 0.212 in SON and 0.209 in JJA. AOD in MAM is significantly higher than other seasons, which
1026 may be related to sandstorms in East Asia, and the reason for the high AOD in winter may be related
1027 to the transportation. The trends of AOD in DJF (-0.0025/10a, p>0.05), MAM (0.0031/10a, p>0.05),
1028 JJA (0) and SON (-0.0006/10a, p>0.05) are not significant. In Eastern China, the multi-year average
1029 AOD is 0.233, with an increasing trend (0.0071/10a, p<0.01). The trend is 0.0151/10a from 1980 to
1030 2006 and -0.0469/10a from 2006 to 2021. The seasonal average AOD ranking from high to low is
1031 JJA (0.284), MAM (0.234), SON (0.230) and DJF (0.183). The AOD trends in DJF (0.0093/10a,
1032 p<0.01), MAM (0.0092/10a, p<0.01), JJA (0.0038/10a, p>0.05) and SON (0.0065/10a, p<0.05) are
1033 all positive but the trend in JJA does not pass the significance test. We can see that there are three
1034 stages of changes in AOD: 1980-2005, 2006-2013 and 2014-2021. In the first stage, AOD increased
1035 steadily. In the second stage, AOD maintained a larger positive anomaly accompanied by
1036 oscillations. The third stage experienced a rapid decline, reaching the level of the 1980s by 2021.
1037 The increasing trend of AOD before 2006 may be due to the significant increase in industrial activity,

1038 and after 2013, the significant decrease is closely related to the implementation of air quality-related
 1039 laws and regulations, along with adjustments in the energy structure (Hu et al., 2018; Cherian and
 1040 Quaas, 2020).

1041 India is a high aerosol loading area. The multi-year average AOD is 0.255, with an upward trend
 1042 (0.0096/10a, $p < 0.01$) from 1980 to 2021. Dust and biomass burning has an influence on AOD level.
 1043 There are three stages: 1980-1997 (0.0032/10a, $p < 0.01$), 1997-2005 (-0.0420/10a, $p < 0.01$), 2005-
 1044 2021 (0.0481/10a, $p < 0.01$). Although the trend is downward in the second stage, the larger positive
 1045 trend is in the third stage. The seasonal average AOD values are 0.237 in DJF, 0.258 in MAM, 0.269
 1046 in JJA, and 0.256 in SON. The largest AOD is in JJA. In winter and autumn, it affected by biomass
 1047 burning, and in spring and summer, it is also affected by dust, transported from the Sahara under
 1048 during the monsoon period (Remer et al., 2008). The trends in DJF (0.0152/10a, $p < 0.01$), MAM
 1049 (0.0091/10a, $p < 0.01$), JJA (0.0025/10a, $p > 0.05$), and SON (0.0107/10a, $p < 0.05$) are positive. There
 1050 largest trend is in winter.

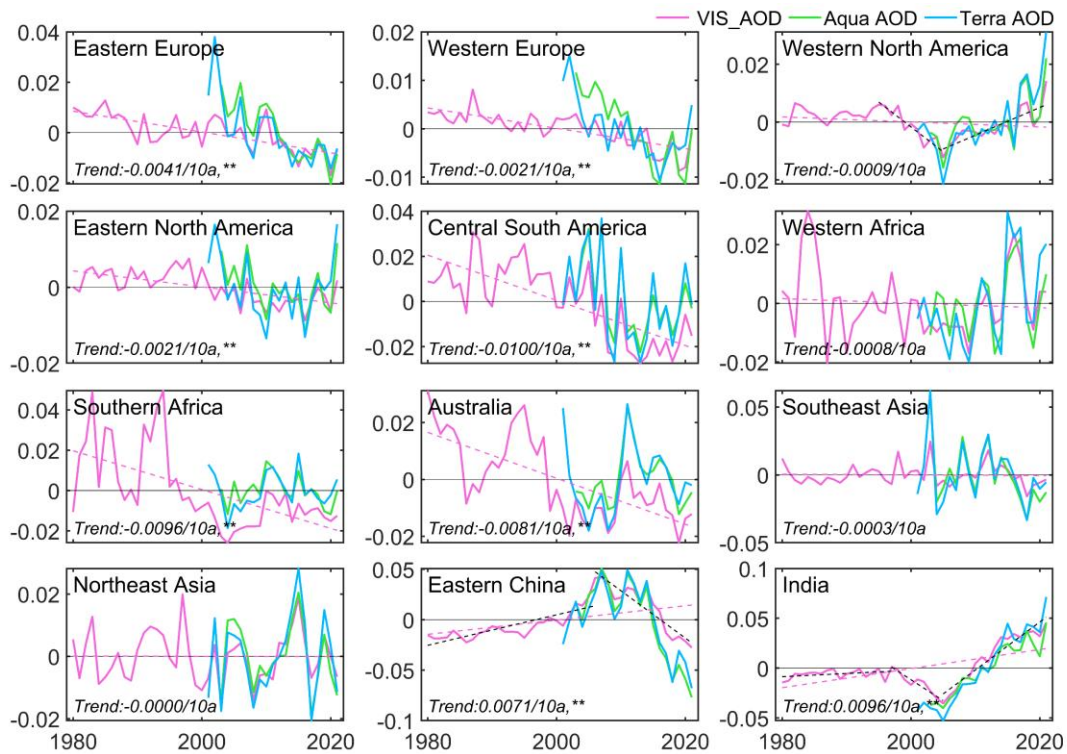
1051 To summarize, there are significant differences in the spatial distribution, annual trends, and
 1052 seasonal trends of AOD across different regions from 1980 to 2021. The high aerosol loadings from
 1053 1980 to 2021 are in West Africa, India and Asia, and low aerosol loading regions are in Europe,
 1054 Western North America, and Australia. Eastern China and India show an increasing trend, Southeast
 1055 Asia and Northeast Asia show no significant trend, and the other regions show downward trends.
 1056 However, not all regional seasonal trends are consistent with their annual trends. The results in this
 1057 study have supplemented the long-term trend and distribution of AOD over land.



1058

1059 **Figure 13-15:** Annual and seasonal averages of AOD in 12 regions during 1980-2021.

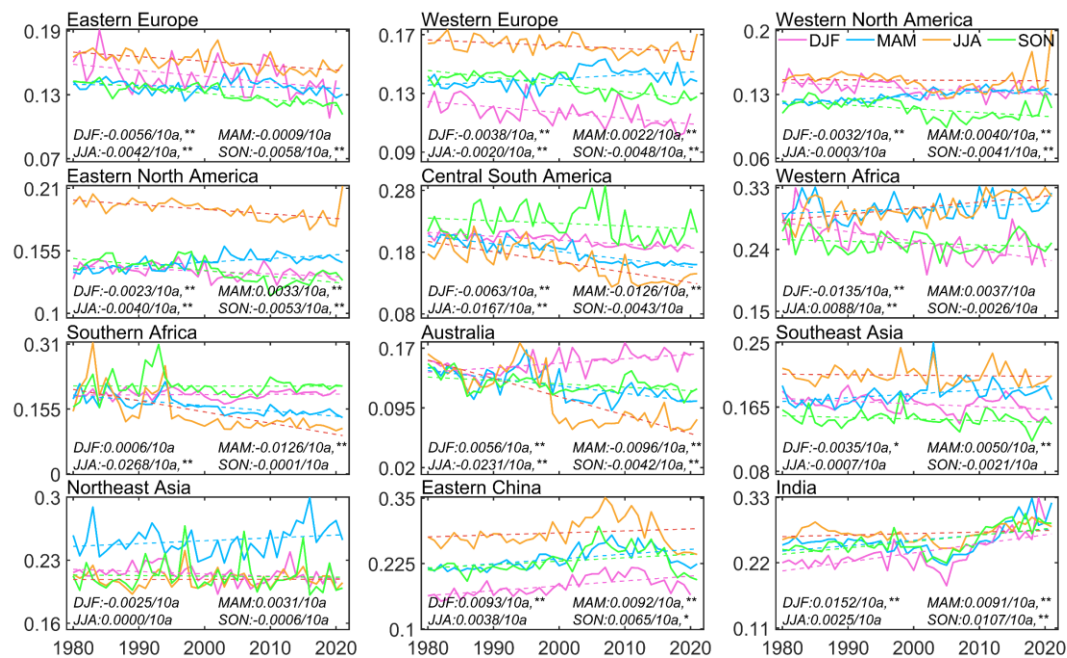
1060



1061

1062 **Figure 14-16:** Annual averages of monthly anomaly gridded VIS_AOD (pink line), Aqua (green
 1063 line), and Terra (blue line) MODIS AOD in 12 regions. The dotted line is the trend line.

1064



1065

1066 **Figure 15-17:** Seasonal averages of gridded VIS_AOD during 1980 to 2021 in 12 regions (Eastern
 1067 Europe, Western Europe, Western North America, Eastern North America, Central South America,
 1068 Western Africa, Southern Africa, Australia, Southeast Asia, Northeast Asia, Eastern China, and

1069 India). The dotted line is the trend line.

1070 **4 Data availability**

1071 The visibility-derived AOD at station and grid scales over global land ~~from 1980 to 2021~~ are
1072 available at National Tibetan Plateau / Third Pole Environment Data Center,
1073 (<https://doi.org/10.11888/Atmos.tpsc.300822>) (Hao et al., 2023).

1074 We provide the station-scale AOD from 1959 to 2021. Due to a small number and sparse
1075 meteorological stations prior to 1980, we only provide the gridded AOD from 1980 to 2021. In order
1076 to keep consistency in time scale, the time range we describe in this study is from 1980 to 2021. The
1077 following is a description to the station and gridded VIS_AOD dataset.

1078 The station-scale AOD files are in ‘Station_Daily_AOD_1959_2021.zip’. The station-scale AOD
1079 files can be directly opened by a text program (such as Notepad). The details station information is
1080 in the file of ‘0A0A-Station_Information.txt’. There are eight columns in each text file, separated
1081 by commas and column names are Datetime, TEMP (°C), DEW (°C), RH (%), WS (m/s), SLP (hPa),
1082 DRYVIS (km), and VIS_AOD (550nm). The 2-7th column names are temperature (unit: °C), dew
1083 temperature (unit: °C), relative humidity (unit: %), wind speed (unit: m/s), sea level pressure (unit:
1084 hPa), and dry visibility (unit: km).

1085 The gridded AOD is in the file of ‘Gridded Monthly AOD_1980_2021.nc’ with a NETCDF4
1086 format. There are three variables: ‘VIS_AOD’ (AOD derived from visibility), ‘W95CI’ (the width
1087 of the 95% confidence interval), and ‘QA_FLAG’ (quality flag for VIS_AOD). We classify the
1088 quality of VIS_AOD into three levels based on ‘W95CI’: (1) High quality (QA_FLAG=1):
1089 W95CI<=0.03; (2) Medium quality (QA_FLAG=2), 0.03<W95CI<=0.06; and Low quality
1090 (QA_FLAG=3), W95CI>0.06. The more details are in ‘0A0B-ReadMe.txt’.

1091

1092 **5 Conclusions**

1093 In this study, we employed a machine learning technique to derive AOD for over 5000 land stations
1094 worldwide, based on satellite data, visibility, and related meteorological variables parameters. The
1095 target is Aqua MODIS AOD. Monthly AOD was-is interpolated into a 0.5° grid using ordinary
1096 kriging with area weighting. ~~The method was trained with Aqua MODIS AOD.~~ The accuracy and
1097 performance of the derived AOD were-are assessed and validated against Terra MODIS AOD as
1098 well as AERONET ground-based observations and MRRRA-2 of AOD for the corresponding
1099 stations. ~~Evaluation of~~ The gridded AOD was-is evaluated conducted usingby Aqua and Terra
1100 MODIS AOD and a 95% confidence interval is calculated. We obtained daily AOD (550nm) for-at
1101 5032 global land stations from 1980 to 2021, as well as monthly gridded AOD. The two datasets
1102 complement the shortcomings of AOD data in terms of time scale and spatial coverage. Finally, the
1103 spatiotemporal variation in AOD was-is analyzed for global land, the Southern Hemisphere, the
1104 Northern Hemisphere, and 12 regions in the past 42 years. Several key findings have been obtained
1105 given in this study as follows.

1106 **1. Modeling and gridding evaluation.** The mean RMSE, MAE, and R of all stations are 0.078,
1107 0.044, and 0.750, respectively. The RMSE of 93% stations is less than 0.11, the MAE of 91% is less
1108 than 0.06, and the R of 88% is greater than 0.7, respectively. Compared to Aqua and Terra, the
1109 average biases of gridded AOD are 3.3% and 1.9%, and the spatial correlation coefficients are 0.80
1110 and 0.79, with the zonal correlation coefficients of 0.99 and 0.99 and the meridional correlation
1111 coefficients of 0.99 and 0.90.

1112 **2. Model validation.** For the daily scale, the R, RMSE and MAE of between VIS_AOD and Aqua
1113 AOD is 0.799, 0.079 and 0.044, respectively. The percentage of sample point falling within the EE
1114 envelopes is 84.12%. The R between VIS_AOD and Terra AOD is 0.542, with a RMSE of 0.125
1115 and MAE of 0.078. The percentage falling within the EE envelopes is 64.76%. The R between
1116 VIS_AOD and AERONET AOD is 0.546, with a RMSE of 0.186 and MAE of 0.099. The percentage
1117 falling within the EE envelopes is 57.87%. For the monthly and annual scales, RMSE and MAE
1118 show a significant decrease between VIS_AOD and Aqua, Terra, and AERONET AOD, and R and
1119 percentages falling within EE show a significant increase.

1120 **3. Error analysis.** The average bias is 0.015 (AOD < 0.1), with 83% of data within the EE envelopes.
1121 As pollution level increases, the negative mean bias becomes significant and the underestimation
1122 increases. There is a negative bias in the low elevation (<=0.5km) with a percentage of 60%-64%
1123 falling within the EE envelopes and a positive bias in high elevation (0.5-1.2km) with a percentage
1124 of 50%-65% falling within the EE envelopes. The elevation of AERONET's site caused a bias in
1125 high elevation. When the elevation difference is negative (the elevation of the meteorological station
1126 is lower than that of the AERONET site), there is a significant positive bias. When the difference is
1127 positive, the mean bias approaches 0 or is positive. The bias does not change significantly with
1128 increasing distance between the meteorological station and AERONET site.

1129 **4. Global land AOD.** The global, NH, and SH AOD values from 1980 to 2021 are 0.161 ± 0.074 ,
1130 0.158 ± 0.076 , and 0.173 ± 0.059 , respectively. Trends in AOD for the global, NH, and SH
1131 demonstrate a decreasing trend of $-0.0026/10a$, $-0.0018/10a$, and $-0.0059/10a$, respectively ($p < 0.01$).
1132 The seasonal AOD ranking from high to low is JJA > MAM > DJF > SON over the global land and in
1133 the NH, while in the SH, it is DJF > JJA > MAM > SON. The largest declining trends are observed in
1134 NH summer and SH winter.

1135 **5.4. Regional AOD.** From 1980 to 2021, regions with high aerosol loadings (AOD > 0.2) were found
1136 in West Africa, Northeast Asia, Eastern China, and India. Regions with moderate aerosol loadings
1137 (AOD between 0.15 and 0.2) are Eastern North America, Central South America, South Africa, and
1138 Southeast Asia. Eastern Europe, Western Europe, Western North America, and Australia are regions
1139 with low aerosol loadings (AOD < 0.15). The trends are $-0.0041/10a$, $-0.0021/10a$, $-0.0009/10a$, $-$
1140 $0.0021/10a$, $-0.0100/10a$, $-0.0008/10a$, $-0.0096/10a$, $-0.0081/10a$, $-0.0003/10a$, $-0.0000/10a$, $-$
1141 $0.0071/10a$, and $0.0096/10a$ in Eastern Europe, Western Europe, Western North America, Eastern
1142 North America, Central South America, Western Africa, Southern Africa, Australia, Southeast Asia,
1143 Northeast Asia, Eastern China, and India, respectively.

1144 **Competing interests**

1145 The contact author has declared that none of the authors has any competing interests.

1146 Acknowledgments

1147 This work ~~was-is~~ supported by the National Key Research & Development Program of China
1148 (2022YFF0801302) and the National Natural Science Foundation of China (41930970). The hourly
1149 visibility data ~~were-are~~ downloaded from <https://mesonet.agron.iastate.edu/ASOS>. The Aerosol
1150 Robotic Network (AERONET) 15-minute aerosol optical depth (AOD) data ~~were-are~~ downloaded
1151 from which can be downloaded from <https://aeronet.gsfc.nasa.gov>. The MODIS AOD data ~~were-are~~
1152 downloaded from <https://ladsweb.modaps.eosdis.nasa.gov>.

1153

1154 References

- 1155 Ackerman, A. S., Hobbs, P. V., and Toon, O. B.: A model for particle microphysics, turbulent mixing,
1156 and radiative transfer in the stratocumulus-topped marine boundary layer and comparisons with
1157 measurements, *J. Atmos. Sci.*, 52, 1204-1236, [https://doi.org/10.1175/1520-
1158 0469\(1995\)052<1204:AMFPMT>2.0.CO;2](https://doi.org/10.1175/1520-0469(1995)052<1204:AMFPMT>2.0.CO;2), 1995.
- 1159 Albrecht, B. A.: Aerosols, cloud microphysics, and fractional cloudiness, *Science*, 245, 1227-1230,
1160 <https://doi.org/10.1126/science.245.4923.1227>, 1989.
- 1161 Anderson, T. L., Charlson, R. J., Bellouin, N., Boucher, O., Chin, M., Christopher, S. A., Haywood, J.,
1162 Kaufman, Y. J., Kinne, S., Ogren, J. A., Remer, L. A., Takemura, T., Tanre, D., Torres, O., Trepte, C. R.,
1163 Wielicki, B. A., Winker, D. M., and Yu, H. B.: An "A-Train" strategy for quantifying direct climate
1164 forcing by anthropogenic aerosols, *B. Am. Meteorol. Soc.*, 86, 1795+, [https://doi.org/10.1175/Bams-86-
1165 12-1795](https://doi.org/10.1175/Bams-86-12-1795), 2005.
- 1166 Andersson, S. M., Martinsson, B. G., Vernier, J.-P., Friberg, J., Brenninkmeijer, C. A., Hermann, M., Van
1167 Velthoven, P. F., and Zahn, A.: Significant radiative impact of volcanic aerosol in the lowermost
1168 stratosphere, *Nat. Commun.*, 6, 7692, <https://doi.org/10.1038/ncomms8692>, 2015.
- 1169 Andrews, E., Sheridan, P. J., Ogren, J. A., Hageman, D., Jefferson, A., Wendell, J., Alástuey, A., Alados-
1170 Arboledas, L., Bergin, M., and Ealo, M.: Overview of the NOAA/ESRL federated aerosol network, *B.*
1171 *Am. Meteorol. Soc.*, 100, 123-135, <https://doi.org/10.1175/BAMS-D-17-0175.1>, 2019.
- 1172 Bergstrom, R. W., Pilewskie, P., Russell, P. B., Redemann, J., Bond, T. C., Quinn, P. K., and Sierau, B.:
1173 Spectral absorption properties of atmospheric aerosols, *Atmos. Chem. Phys.*, 7, 5937-5943,
1174 <https://doi.org/10.5194/acp-7-5937-2007>, 2007.
- 1175 Berk, R. A.: Classification and Regression Trees (CART), in: *Statistical Learning from a Regression*
1176 *Perspective*, Springer New York, New York, NY, 1-65, https://doi.org/10.1007/978-0-387-77501-2_3,
1177 2008.
- 1178 Bescond, A., Yon, J., Girasole, T., Jouen, C., Rozé, C., and Coppalle, A.: Numerical investigation of the
1179 possibility to determine the primary particle size of fractal aggregates by measuring light depolarization,
1180 *J. Quant. Spectrosc. Ra.*, 126, 130-139, <https://doi.org/10.1016/j.jqsrt.2012.10.011>, 2013.
- 1181 Boers, R., van Weele, M., van Meijgaard, E., Savenije, M., Siebesma, A. P., Bosveld, F., and Stammes,
1182 P.: Observations and projections of visibility and aerosol optical thickness (1956-2100) in the
1183 Netherlands: impacts of time-varying aerosol composition and hygroscopicity, *Environ. Res. Lett.*, 10,
1184 <https://doi.org/10.1088/1748-9326/10/1/015003>, 2015.
- 1185 Bokoye, A. I., Royer, A., O'Neil, N., Cliche, P., Fedosejevs, G., Teillet, P., and McArthur, L.:

1186 Characterization of atmospheric aerosols across Canada from a ground-based sunphotometer network:
1187 AEROCAN, *Atmos. Ocean*, 39, 429-456, <https://doi.org/10.1080/07055900.2001.9649687>, 2001.

1188 Bösenberg, J. and Matthias, V.: EARLINET: A European Aerosol Research Lidar Network to Establish
1189 an Aerosol Climatology, Max Planck Institut Fur Meteorologie, 2003.

1190 Bright, J. M. and Gueymard, C. A.: Climate-specific and global validation of MODIS Aqua and Terra
1191 aerosol optical depth at 452 AERONET stations, *Sol. Energy*, 183, 594-605,
1192 <https://doi.org/10.1016/j.solener.2019.03.043>, 2019.

1193 Browne, M. W.: Cross-validation methods, *J. Math. Psychol.*, 44, 108-132,
1194 <https://doi.org/10.1006/jmps.1999.1279>, 2000.

1195 Calvo, A. I., Alves, C., Castro, A., Pont, V., Vicente, A. M., and Fraile, R.: Research on aerosol sources
1196 and chemical composition: Past, current and emerging issues, *Atmos. Res.*, 120, 1-28,
1197 <https://doi.org/10.1016/j.atmosres.2012.09.021>, 2013.

1198 Chafe, Z. A., Brauer, M., Klimont, Z., Van Dingenen, R., Mehta, S., Rao, S., Riahi, K., Dentener, F., and
1199 Smith, K. R.: Household Cooking with Solid Fuels Contributes to Ambient PM_{2.5} Air Pollution and the
1200 Burden of Disease, *Environ. Health Persp.*, 122, 1314-1320, <https://doi.org/10.1289/ehp.1206340>, 2014.

1201 Chazette, P., David, C., Lefrère, J., Godin, S., Pelon, J., and Mégie, G.: Comparative lidar study of the
1202 optical, geometrical, and dynamical properties of stratospheric post-volcanic aerosols, following the
1203 eruptions of El Chichon and Mount Pinatubo, *J. Geophys. Res-Atmos.*, 100, 23195-23207,
1204 <https://doi.org/10.1029/95JD02268>, 1995.

1205 Che, H., Zhang, X., Chen, H., Damiri, B., Goloub, P., Li, Z., Zhang, X., Wei, Y., Zhou, H., Dong, F., Li,
1206 D., and Zhou, T.: Instrument calibration and aerosol optical depth validation of the China Aerosol Remote
1207 Sensing Network, *J. Geophys. Res-Atmos.*, 114, <https://doi.org/10.1029/2008jd011030>, 2009.

1208 Che, H., Xia, X., Zhu, J., Li, Z., Dubovik, O., Holben, B., Goloub, P., Chen, H., Estelles, V., Cuevas-
1209 Agullo, E., Blarel, L., Wang, H., Zhao, H., Zhang, X., Wang, Y., Sun, J., Tao, R., Zhang, X., and Shi, G.:
1210 Column aerosol optical properties and aerosol radiative forcing during a serious haze-fog month over
1211 North China Plain in 2013 based on ground-based sunphotometer measurements, *Atmos. Chem. Phys.*,
1212 14, 2125-2138, <https://doi.org/10.5194/acp-14-2125-2014>, 2014.

1213 Chen, A., Zhao, C., and Fan, T.: Spatio-temporal distribution of aerosol direct radiative forcing over mid-
1214 latitude regions in north hemisphere estimated from satellite observations, *Atmos. Res.*, 266, 105938,
1215 <https://doi.org/10.1016/j.atmosres.2021.105938>, 2022.

1216 Chen, D., Ou, T., Gong, L., Xu, C.-Y., Li, W., Ho, C.-H., and Qian, W.: Spatial Interpolation of Daily
1217 Precipitation in China: 1951-2005, *Adv. Atmos. Sci.*, 27, 1221-1232, <https://doi.org/10.1007/s00376-010-9151-y>, 2010.

1219 Cherian, R. and Quaas, J.: Trends in AOD, clouds, and cloud radiative effects in satellite data and CMIP5
1220 and CMIP6 model simulations over aerosol source regions, *Geophys. Res. Lett.*, 47, e2020GL087132,
1221 <https://doi.org/10.1029/2020GL087132>, 2020.

1222 Chin, M., Diehl, T., Tan, Q., Prospero, J., Kahn, R., Remer, L., Yu, H., Sayer, A., Bian, H., and
1223 Geogdzhayev, I.: Multi-decadal aerosol variations from 1980 to 2009: a perspective from observations
1224 and a global model, *Atmos. Chem. Phys.*, 14, 3657-3690, <https://doi.org/10.5194/acp-14-3657-2014>,
1225 2014.

1226 Chu, D., Kaufman, Y., Ichoku, C., Remer, L., Tanré, D., and Holben, B.: Validation of MODIS aerosol
1227 optical depth retrieval over land, *Geophys. Res. Lett.*, 29, MOD2-1-MOD2-4,
1228 <https://doi.org/10.1029/2001GL013205>, 2002.

1229 Chuang, P.-J. and Huang, P.-Y.: B-VAE: a new dataset balancing approach using batched Variational

1230 AutoEncoders to enhance network intrusion detection, *J. Supercomput.*, [https://doi.org/10.1007/s11227-](https://doi.org/10.1007/s11227-023-05171-w)
1231 [023-05171-w](https://doi.org/10.1007/s11227-023-05171-w), 2023.

1232 Deuzé, J., Goloub, P., Herman, M., Marchand, A., Perry, G., Susana, S., and Tanré, D.: Estimate of the
1233 aerosol properties over the ocean with POLDER, *J. Geophys. Res-Atmos.*, 105, 15329-15346,
1234 <https://doi.org/10.1029/2000JD900148>, 2000.

1235 Dhanya, R., Paul, I. R., Akula, S. S., Sivakumar, M., and Nair, J. J.: F-test feature selection in Stacking
1236 ensemble model for breast cancer prediction, *Procedia. Comput. Sci.*, 171, 1561-1570,
1237 <https://doi.org/10.1016/j.procs.2020.04.167>, 2020.

1238 Diner, D. J., Beckert, J. C., Reilly, T. H., Bruegge, C. J., Conel, J. E., Kahn, R. A., Martonchik, J. V.,
1239 Ackerman, T. P., Davies, R., and Gerstl, S. A. W.: Multi-angle Imaging SpectroRadiometer (MISR)
1240 instrument description and experiment overview, *Ieee T. Geosci. Remote.*, 98, 1072-1087,
1241 <https://doi.org/10.1109/36.700992>, 1998.

1242 Dong, Y., Li, J., Yan, X., Li, C., Jiang, Z., Xiong, C., Chang, L., Zhang, L., Ying, T., and Zhang, Z.:
1243 Retrieval of aerosol single scattering albedo using joint satellite and surface visibility measurements,
1244 *Remote Sens. Environ.*, 294, 113654, <https://doi.org/10.1016/j.rse.2023.113654>, 2023.

1245 Dubovik, Oleg, Holben, Brent, Eck, Thomas, F., Smirnov, Alexander, and Kaufman: Variability of
1246 Absorption and Optical Properties of Key Aerosol Types Observed in Worldwide Locations, *J. Atmos.*
1247 *Sci.*, 59, 590-590, [https://doi.org/10.1175/1520-0469\(2002\)059<0590:VOAAOP>2.0.CO;2](https://doi.org/10.1175/1520-0469(2002)059<0590:VOAAOP>2.0.CO;2), 2002a.

1248 Dubovik, O., Smirnov, A., Holben, B. N., King, M. D., Kaufman, Y. J., Eck, T. F., and Slutsker, I.:
1249 Accuracy assessments of aerosol optical properties retrieved from Aerosol Robotic Network (AERONET)
1250 Sun and sky radiance measurements, *J. Geophys. Res-Atmos.*, 105, 9791-9806,
1251 <https://doi.org/10.1029/2000jd900040>, 2000.

1252 Dubovik, O., Holben, B., Eck, T. F., Smirnov, A., Kaufman, Y. J., King, M. D., Tanré, D., and Slutsker,
1253 I.: Variability of absorption and optical properties of key aerosol types observed in worldwide locations,
1254 *J. Atmos. Sci.*, 59, 590-608, [https://doi.org/10.1175/1520-0469\(2002\)059<0590:VOAAOP>2.0.CO;2](https://doi.org/10.1175/1520-0469(2002)059<0590:VOAAOP>2.0.CO;2),
1255 2002b.

1256 Eck, T. F., Holben, B. N., Reid, J. S., Sinyuk, A., Giles, D. M., Arola, A., Slutsker, I., Schafer, J. S.,
1257 Sorokin, M. G., and Smirnov, A.: The extreme forest fires in California/Oregon in 2020: Aerosol optical
1258 and physical properties and comparisons of aged versus fresh smoke, *Atmos. Environ.*, 305, 119798,
1259 <https://doi.org/10.1016/j.atmosenv.2023.119798>, 2023.

1260 Elterman, L.: Relationships between vertical attenuation and surface meteorological range, *Appl. Optics*,
1261 9, 1804-1810, <https://doi.org/10.1364/AO.9.001804>, 1970.

1262 Fan, H., Zhao, C., Yang, Y., and Yang, X.: Spatio-Temporal Variations of the
1263 PM_{2.5}/PM₁₀ Ratios and Its Application to Air Pollution Type Classification
1264 in China, *Front. Environ. Sci.*, 9, <https://doi.org/10.3389/fenvs.2021.692440>, 2021.

1265 Fernández, A., Garcia, S., Herrera, F., and Chawla, N. V.: SMOTE for learning from imbalanced data:
1266 progress and challenges, marking the 15-year anniversary, *J. Artif. Intell. Res.*, 61, 863-905,
1267 <https://doi.org/10.1613/jair.1.11192>, 2018.

1268 Forster, P., Ramaswamy, V., Artaxo, P., Bernsten, T., Betts, R., Fahey, D. W., Haywood, J., Lean, J., Lowe,
1269 D. C., and Myhre, G.: Changes in atmospheric constituents and in radiative forcing, *Climate Change*
1270 2007: The Physical Science Basis. Contribution of Working Group I to the 4th Assessment Report of the
1271 Intergovernmental Panel on Climate Change, 2007.

1272 Gelaro, R., McCarty, W., Suárez, M. J., Todling, R., Molod, A., Takacs, L., Randles, C. A., Darmenov,
1273 A., Bosilovich, M. G., Reichle, R., Wargan, K., Coy, L., Cullather, R., Draper, C., Akella, S., Buchard,

1274 V., Conaty, A., da Silva, A. M., Gu, W., Kim, G.-K., Koster, R., Lucchesi, R., Merkova, D., Nielsen, J.
1275 E., Partyka, G., Pawson, S., Putman, W., Rienecker, M., Schubert, S. D., Sienkiewicz, M., and Zhao, B.:
1276 The Modern-Era Retrospective Analysis for Research and Applications, Version 2 (MERRA-2), J.
1277 Climate, 30, 5419-5454, <https://doi.org/10.1175/JCLI-D-16-0758.1>, 2017.

1278 Giglio, L., Randerson, J. T., and Van Der Werf, G. R.: Analysis of daily, monthly, and annual burned area
1279 using the fourth-generation global fire emissions database (GFED4), J. Geophys. Res-Bioge., 118, 317-
1280 328, <https://doi.org/10.1002/jgrg.20042>, 2013.

1281 Giles, D. M., Sinyuk, A., Sorokin, M. G., Schafer, J. S., Smirnov, A., Slutsker, I., Eck, T. F., Holben, B.
1282 N., Lewis, J. R., Campbell, J. R., Welton, E. J., Korkin, S. V., and Lyapustin, A. I.: Advancements in the
1283 Aerosol Robotic Network (AERONET) Version 3 database – automated near-real-time quality control
1284 algorithm with improved cloud screening for Sun photometer aerosol optical depth (AOD) measurements,
1285 Atmos. Meas. Tech., 12, 169-209, <https://doi.org/10.5194/amt-12-169-2019>, 2019.

1286 Goovaerts, P.: Geostatistical approaches for incorporating elevation into the spatial interpolation of
1287 rainfall, Journal of Hydrology, 228, 113-129, [https://doi.org/10.1016/s0022-1694\(00\)00144-x](https://doi.org/10.1016/s0022-1694(00)00144-x), 2000.

1288 Gras, J., Jensen, J., Okada, K., Ikegami, M., Zaizen, Y., and Makino, Y.: Some optical properties of smoke
1289 aerosol in Indonesia and tropical Australia, Geophys. Res. Lett., 26, 1393-1396,
1290 <https://doi.org/10.1029/1999GL900275>, 1999.

1291 Guerrero-Rascado, J. L., Landulfo, E., Antuña, J. C., Barbosa, H. d. M. J., Barja, B., Bastidas, Á. E.,
1292 Bedoya, A. E., da Costa, R. F., Estevan, R., and Forno, R.: Latin American Lidar Network (LALINET)
1293 for aerosol research: Diagnosis on network instrumentation, J. Atmos. Sol-Terr. Phys., 138, 112-120,
1294 <https://doi.org/10.1016/j.jastp.2016.01.001>, 2016.

1295 Guo, J., Zhang, J., Yang, K., Liao, H., Zhang, S., Huang, K., Lv, Y., Shao, J., Yu, T., and Tong, B.:
1296 Investigation of near-global daytime boundary layer height using high-resolution radiosondes: first
1297 results and comparison with ERA5, MERRA-2, JRA-55, and NCEP-2 reanalyses, Atmos. Chem. Phys.,
1298 21, 17079-17097, <https://doi.org/10.5194/acp-21-17079-2021>, 2021.

1299 Hao, H., Wang, K., and Wu, G.: Visibility-derived aerosol optical depth over global land (1980-2021),
1300 National Tibetan Plateau Data Center [dataset], <https://doi.org/10.11888/Atmos.tpdc.300822>, 2023.

1301 He, H., Bai, Y., Garcia, E. A., and Li, S.: ADASYN: Adaptive synthetic sampling approach for
1302 imbalanced learning, IEEE World Congress on Computational Intelligence, 1322-1328,
1303 <https://doi.org/10.1109/IJCNN.2008.4633969>, 2008.

1304 Hersbach, H., Bell, B., Berrisford, P., Hirahara, S., Horányi, A., Muñoz-Sabater, J., Nicolas, J., Peubey,
1305 C., Radu, R., and Schepers, D.: The ERA5 global reanalysis, Q. J. Roy. Meteor. Soc., 146, 1999-2049,
1306 <https://doi.org/10.1002/qj.3803>, 2020.

1307 Hersey, S. P., Garland, R. M., Crosbie, E., Shingler, T., Sorooshian, A., Piketh, S., and Burger, R.: An
1308 overview of regional and local characteristics of aerosols in South Africa using satellite, ground, and
1309 modeling data, Atmos. Chem. Phys., 15, 4259-4278, <https://doi.org/10.5194/acp-15-4259-2015>, 2015.

1310 Hirono, M. and Shibata, T.: Enormous increase of stratospheric aerosols over Fukuoka due to volcanic
1311 eruption of El Chichon in 1982, Geophys. Res. Lett., 10, 152-154,
1312 <https://doi.org/10.1029/GL010i002p00152>, 1983.

1313 Hofmann, D., Barnes, J., O'Neill, M., Trudeau, M., and Neely, R.: Increase in background stratospheric
1314 aerosol observed with lidar at Mauna Loa Observatory and Boulder, Colorado, Geophys. Res. Lett., 36,
1315 <https://doi.org/10.1029/2009GL039008>, 2009.

1316 Holben, B. N., Eck, T. F., Slutsker, I., Tanre, D., Buis, J. P., Setzer, A., Vermote, E., Reagan, J. A.,
1317 Kaufman, Y. J., Nakajima, T., Lavenu, F., Jankowiak, I., and Smirnov, A.: AERONET - A federated

1318 instrument network and data archive for aerosol characterization, *Remote Sens. Environ.*, 66, 1-16,
1319 [https://doi.org/10.1016/s0034-4257\(98\)00031-5](https://doi.org/10.1016/s0034-4257(98)00031-5), 1998.

1320 Hsu, N., Gautam, R., Sayer, A., Bettenhausen, C., Li, C., Jeong, M., Tsay, S.-C., and Holben, B.: Global
1321 and regional trends of aerosol optical depth over land and ocean using SeaWiFS measurements from
1322 1997 to 2010, *Atmos. Chem. Phys.*, 12, 8037-8053, <https://doi.org/10.5194/acp-12-8037-2012>, 2012.

1323 Hsu, N., Jeong, M. J., Bettenhausen, C., Sayer, A., Hansell, R., Seftor, C., Huang, J., and Tsay, S. C.:
1324 Enhanced Deep Blue aerosol retrieval algorithm: The second generation, *J. Geophys. Res-Atmos.*, 118,
1325 9296-9315, <https://doi.org/10.1002/jgrd.50712>, 2013.

1326 Hsu, N., Lee, J., Sayer, A., Carletta, N., Chen, S. H., Tucker, C., Holben, B., and Tsay, S. C.: Retrieving
1327 near-global aerosol loading over land and ocean from AVHRR, *J. Geophys. Res-Atmos.*, 122, 9968-
1328 9989, <https://doi.org/10.1002/2017JD026932>, 2017.

1329 Hsu, N. C., Tsay, S.-C., King, M. D., and Herman, J. R.: Deep blue retrievals of Asian aerosol properties
1330 during ACE-Asia, *Ieee T. Geosci. Remote.*, 44, 3180-3195, <https://doi.org/10.1109/tgrs.2006.879540>,
1331 2006.

1332 Hu, B., Zhang, X., Sun, R., and Zhu, X.: Retrieval of Horizontal Visibility Using MODIS Data: A Deep
1333 Learning Approach, *Atmosphere-Basel*, 10, <https://doi.org/10.3390/atmos10120740>, 2019.

1334 Hu, K., Kumar, K. R., Kang, N., Boiyo, R., and Wu, J.: Spatiotemporal characteristics of aerosols and
1335 their trends over mainland China with the recent Collection 6 MODIS and OMI satellite datasets, *Environ.*
1336 *Sci. Pollut. R.*, 25, 6909-6927, <https://doi.org/10.1007/s11356-017-0715-6>, 2018.

1337 Husar, R. B., Husar, J. D., and Martin, L.: Distribution of continental surface aerosol extinction based on
1338 visual range data, *Atmos. Environ.*, 34, 5067-5078, [https://doi.org/10.1016/s1352-2310\(00\)00324-1](https://doi.org/10.1016/s1352-2310(00)00324-1),
1339 2000.

1340 IPCC: *Climate Change 2021: The Physical Science Basis*, Cambridge University Press, New York, 2021.

1341 Ivanova, G., Ivanov, V., Kukavskaya, E., and Soja, A.: The frequency of forest fires in Scots pine stands
1342 of Tuva, Russia, *Environ. Res. Lett.*, 5, 015002, <https://doi.org/10.1088/1748-9326/5/1/015002>, 2010.

1343 Kang, Y., Kim, M., Kang, E., Cho, D., and Im, J.: Improved retrievals of aerosol optical depth and fine
1344 mode fraction from GOCI geostationary satellite data using machine learning over East Asia, *Isprs J.*
1345 *Photogramm.*, 183, 253-268, <https://doi.org/10.1016/j.isprsjprs.2021.11.016>, 2022.

1346 Kang, Y., Choi, H., Im, J., Park, S., Shin, M., Song, C.-K., and Kim, S.: Estimation of surface-level NO₂
1347 and O₃ concentrations using TROPOMI data and machine learning over East Asia, *Environ. Pollut.*, 288,
1348 117711, <https://doi.org/10.1016/j.envpol.2021.117711>, 2021.

1349 Karbowska, B. and Zembrzuski, W.: Fractionation and mobility of thallium in volcanic ashes after
1350 eruption of Eyjafjallajökull (2010) in Iceland, *B. Environ. Contam. Tox.*, 97, 37-43,
1351 <https://doi.org/10.1007/s00128-016-1831-6>, 2016.

1352 Kaufman, Y. J. and Boucher, O.: A satellite view of aerosols in the climate system, *Nature*, 419, 215-215,
1353 <https://doi.org/10.1038/nature01091>, 2002.

1354 Kim, D. H., Sohn, B. J., Nakajima, T., Takamura, T., Takemura, T., Choi, B. C., and Yoon, S. C.: Aerosol
1355 optical properties over east Asia determined from ground-based sky radiation measurements, *J. Geophys.*
1356 *Res-Atmos.*, 109, <https://doi.org/10.1029/2003jd003387>, 2004.

1357 Klett, J. D.: Lidar inversion with variable backscatter/extinction ratios, *Appl. Optics*, 24, 1638-1643,
1358 <https://doi.org/10.1364/AO.24.001638>, 1985.

1359 Koelemeijer, R., Homan, C., and Matthijsen, J.: Comparison of spatial and temporal variations of aerosol
1360 optical thickness and particulate matter over Europe, *Atmos. Environ.*, 40, 5304-5315,
1361 <https://doi.org/10.1016/j.atmosenv.2006.04.044>, 2006.

1362 Koschmieder, H.: Theorie der horizontalen Sichtweite, Beitrage zur Physik der freien Atmosphäre, 12,
1363 33-55, 1924.

1364 Krylov, A., McCarty, J. L., Potapov, P., Loboda, T., Tyukavina, A., Turubanova, S., and Hansen, M. C.:
1365 Remote sensing estimates of stand-replacement fires in Russia, 2002–2011, *Environ. Res. Lett.*, 9,
1366 105007, <https://doi.org/10.1088/1748-9326/9/10/105007>, 2014.

1367 Kulmala, M., Vehkamäki, H., Petäjä, T., Dal Maso, M., Lauri, A., Kerminen, V. M., Birmili, W., and
1368 McMurry, P. H.: Formation and growth rates of ultrafine atmospheric particles: A review of observations,
1369 *J. Aerosol Sci.*, 35, 143-176, <https://doi.org/10.1016/j.jaerosci.2003.10.003>, 2004.

1370 Kummu, M., De Moel, H., Salvucci, G., Viviroli, D., Ward, P. J., and Varis, O.: Over the hills and further
1371 away from coast: global geospatial patterns of human and environment over the 20th–21st centuries,
1372 *Environ. Res. Lett.*, 11, 034010, <https://doi.org/10.1088/1748-9326/11/3/034010>, 2016.

1373 Lapen, D. R. and Hayhoe, H. N.: Spatial analysis of seasonal and annual temperature and precipitation
1374 normals in southern Ontario, Canada, *J. Great Lakes Res.*, 29, 529-544, [https://doi.org/10.1016/s0380-1330\(03\)70457-2](https://doi.org/10.1016/s0380-1330(03)70457-2), 2003.

1375
1376 Lee, L. A., Reddington, C. L., and Carslaw, K. S.: On the relationship between aerosol model uncertainty
1377 and radiative forcing uncertainty, *P. Natl. A. Sci.*, 113, 5820-5827,
1378 <https://doi.org/10.1073/pnas.1507050113>, 2016.

1379 Levy, R., Remer, L., Kleidman, R., Mattoo, S., Ichoku, C., Kahn, R., and Eck, T.: Global evaluation of
1380 the Collection 5 MODIS dark-target aerosol products over land, *Atmos. Chem. Phys.*, 10, 10399-10420,
1381 <https://doi.org/10.5194/acp-10-10399-2010>, 2010.

1382 Levy, R. C., Remer, L. A., Mattoo, S., Vermote, E. F., and Kaufman, Y. J.: Second-generation operational
1383 algorithm: Retrieval of aerosol properties over land from inversion of Moderate Resolution Imaging
1384 Spectroradiometer spectral reflectance, *J. Geophys. Res-Atmos.*, 112,
1385 <https://doi.org/10.1029/2006JD007811>, 2007.

1386 Levy, R. C., Mattoo, S., Munchak, L. A., Remer, L. A., Sayer, A. M., Patadia, F., and Hsu, N. C.: The
1387 Collection 6 MODIS aerosol products over land and ocean, *Atmos. Meas. Tech.*, 6, 2989-3034,
1388 <https://doi.org/10.5194/amt-6-2989-2013>, 2013.

1389 Levy, R. C., Mattoo, S., Sawyer, V., Shi, Y., Colarco, P. R., Lyapustin, A. I., Wang, Y., and Remer, L. A.:
1390 Exploring systematic offsets between aerosol products from the two MODIS sensors, *Atmos. Meas. Tech.*,
1391 11, 4073-4092, <https://doi.org/10.5194/amt-11-4073-2018>, 2018.

1392 Li, J., Garshick, E., Hart, J. E., Li, L., Shi, L., Al-Hemoud, A., Huang, S., and Koutrakis, P.: Estimation
1393 of ambient PM_{2.5} in Iraq and Kuwait from 2001 to 2018 using machine learning and remote sensing,
1394 *Environ. Int.*, 151, <https://doi.org/10.1016/j.envint.2021.106445>, 2021.

1395 Li, J., Carlson, B. E., Yung, Y. L., Lv, D., Hansen, J., Penner, J. E., Liao, H., Ramaswamy, V., Kahn, R.
1396 A., Zhang, P., Dubovik, O., Ding, A., Lacis, A. A., Zhang, L., and Dong, Y.: Scattering and absorbing
1397 aerosols in the climate system, *Nat. Rev. Earth. Environ.*, 3, 363-379, <https://doi.org/10.1038/s43017-022-00296-7>, 2022.

1398
1399 Li, S., Chen, L., Huang, G., Lin, J., Yan, Y., Ni, R., Huo, Y., Wang, J., Liu, M., and Weng, H.: Retrieval
1400 of surface PM_{2.5} mass concentrations over North China using visibility measurements and GEOS-Chem
1401 simulations, *Atmos. Environ.*, 222, 117121, <https://doi.org/10.1016/j.atmosenv.2019.117121>, 2020.

1402 Li, Z., Lau, W. M., Ramanathan, V., Wu, G., Ding, Y., Manoj, M., Liu, J., Qian, Y., Li, J., and Zhou, T.:
1403 Aerosol and monsoon climate interactions over Asia, *Rev. Geophys.*, 54, 866-929,
1404 <https://doi.org/10.1002/2015RG000500>, 2016.

1405 Liao, H., Chang, W., and Yang, Y.: Climatic Effects of Air Pollutants over China: A Review, *Adv. Atmos.*

1406 Sci., 32, 115-139, <https://doi.org/10.1007/s00376-014-0013-x>, 2015.

1407 Lin, J. T., van Donkelaar, A., Xin, J. Y., Che, H. Z., and Wang, Y. S.: Clear-sky aerosol optical depth over
1408 East China estimated from visibility measurements and chemical transport modeling, *Atmos. Environ.*,
1409 95, 258-267, <https://doi.org/10.1016/j.atmosenv.2014.06.044>, 2014.

1410 Liu, B., Ma, X., Ma, Y., Li, H., Jin, S., Fan, R., and Gong, W.: The relationship between atmospheric
1411 boundary layer and temperature inversion layer and their aerosol capture capabilities, *Atmos. Res.*, 271,
1412 <https://doi.org/10.1016/j.atmosres.2022.106121>, 2022.

1413 Mahowald, N. M., Ballantine, J. A., Feddema, J., and Ramankutty, N.: Global trends in visibility:
1414 implications for dust sources, *Atmos. Chem. Phys.*, 7, 3309-3339, [https://doi.org/10.5194/acp-7-3309-](https://doi.org/10.5194/acp-7-3309-2007)
1415 [2007](https://doi.org/10.5194/acp-7-3309-2007), 2007.

1416 McNeill, V. F.: Atmospheric Aerosols: Clouds, Chemistry, and Climate, in: *Annu. Rev. Chem. Biomol.*,
1417 edited by: Prausnitz, J. M., *Annual Review of Chemical and Biomolecular Engineering*, 427-444,
1418 <https://doi.org/10.1146/annurev-chembioeng-060816-101538>, 2017.

1419 Mehta, M., Singh, R., Singh, A., and Singh, N.: Recent global aerosol optical depth variations and
1420 trends—A comparative study using MODIS and MISR level 3 datasets, *Remote Sens. Environ.*, 181,
1421 137-150, <https://doi.org/10.1016/j.rse.2016.04.004>, 2016.

1422 Mitra, R., Bajpai, A., and Biswas, K.: ADASYN-assisted machine learning for phase prediction of high
1423 entropy carbides, *Comp. Mater. Sci.*, 223, <https://doi.org/10.1016/j.commatsci.2023.112142>, 2023.

1424 Mortier, A., Gliß, J., Schulz, M., Aas, W., Andrews, E., Bian, H., Chin, M., Ginoux, P., Hand, J., and
1425 Holben, B.: Evaluation of climate model aerosol trends with ground-based observations over the last 2
1426 decades—an AeroCom and CMIP6 analysis, *Atmos. Chem. Phys.*, 20, 13355-13378,
1427 <https://doi.org/10.5194/acp-20-13355-2020>, 2020.

1428 Mukkavilli, S., Prasad, A., Taylor, R., Huang, J., Mitchell, R., Troccoli, A., and Kay, M.: Assessment of
1429 atmospheric aerosols from two reanalysis products over Australia, *Atmos. Res.*, 215, 149-164,
1430 <https://doi.org/10.1016/j.atmosres.2018.08.026>, 2019.

1431 Nagaraja Rao, C., Stowe, L., and McClain, E.: Remote sensing of aerosols over the oceans using AVHRR
1432 data Theory, practice and applications, *Int. J. Remote Sens.*, 10, 743-749,
1433 <https://doi.org/10.1080/01431168908903915>, 1989.

1434 Nakajima, T., Campanelli, M., Che, H., Estellés, V., Irie, H., Kim, S.-W., Kim, J., Liu, D., Nishizawa, T.,
1435 and Pandithurai, G.: An overview of and issues with sky radiometer technology and SKYNET, *Atmos.*
1436 *Meas. Tech.*, 13, 4195-4218, <https://doi.org/10.5194/amt-13-4195-2020>, 2020.

1437 NOAA, DOD, FAA, and USN: Automated Surface Observing System (ASOS) User's Guide, 1998.

1438 O'Reilly, J. E., Maritorena, S., Mitchell, B. G., Siegel, D. A., Carder, K. L., Garver, S. A., Kahru, M., and
1439 McClain, C.: Ocean color chlorophyll algorithms for SeaWiFS, *J. Geophys. Res.*, 103, 24937-24953,
1440 <https://doi.org/10.1029/98jc02160>, 1998.

1441 Pebesma, E. J.: Multivariable geostatistics in S: the gstat package, *Comput. Geosci.*, 30, 683-691,
1442 <https://doi.org/10.1016/j.cageo.2004.03.012>, 2004.

1443 Qiu, J. and Lin, Y.: A parameterization model of aerosol optical depths in China, *Acta. Meteorol. Sin.*,
1444 59, 368-372, <https://doi.org/10.11676/qxxb2001.039>, 2001.

1445 Ramanathan, V., Crutzen, P. J., Kiehl, J., and Rosenfeld, D.: Aerosols, climate, and the hydrological cycle,
1446 *Science*, 294, 2119-2124, <https://doi.org/10.1126/science.1064034>, 2001.

1447 Remer, L. A., Kleidman, R. G., Levy, R. C., Kaufman, Y. J., Tanre, D., Mattoo, S., Martins, J. V., Ichoku,
1448 C., Koren, I., Yu, H., and Holben, B. N.: Global aerosol climatology from the MODIS satellite sensors,
1449 *J. Geophys. Res-Atmos.*, 113, <https://doi.org/10.1029/2007jd009661>, 2008.

1450 Remer, L. A., Kaufman, Y. J., Tanre, D., Mattoo, S., Chu, D. A., Martins, J. V., Li, R. R., Ichoku, C.,
1451 Levy, R. C., Kleidman, R. G., Eck, T. F., Vermote, E., and Holben, B. N.: The MODIS aerosol algorithm,
1452 products, and validation, *J. Atmos. Sci.*, 62, 947-973, <https://doi.org/10.1175/jas3385.1>, 2005.

1453 Salomonson, V. V., Barnes, W. L., Maymon, P. W., Montgomery, H. E., and Ostrow, H.: MODIS:
1454 advanced facility instrument for studies of the Earth as a system, *Ieee T. Geosci. Remote.*, 27, 145-153,
1455 <https://doi.org/10.1109/36.20292>, 1987.

1456 Sawamura, P., Vernier, J. P., Barnes, J. E., Berkoff, T. A., Welton, E. J., Alados-Arboledas, L., Navas-
1457 Guzmán, F., Pappalardo, G., Mona, L., and Madonna, F.: Stratospheric AOD after the 2011 eruption of
1458 Nabro volcano measured by lidars over the Northern Hemisphere, *Environ. Res. Lett.*, 7, 34013-
1459 34021(34019), <https://doi.org/10.1088/1748-9326/7/3/034013>, 2012.

1460 Schutgens, N., Tsyro, S., Gryspeerd, E., Goto, D., Weigum, N., Schulz, M., and Stier, P.: On the spatio-
1461 temporal representativeness of observations, *Atmos. Chem. Phys.*, 17, 9761-9780,
1462 <https://doi.org/10.5194/acp-17-9761-2017>, 2017.

1463 Singh, A., Mahata, K. S., Rupakheti, M., Junkermann, W., Panday, A. K., and Lawrence, M. G.: An
1464 overview of airborne measurement in Nepal–Part 1: Vertical profile of aerosol size, number, spectral
1465 absorption, and meteorology, *Atmos. Chem. Phys.*, 19, 245-258, [https://doi.org/10.5194/acp-19-245-](https://doi.org/10.5194/acp-19-245-2019)
1466 [2019](https://doi.org/10.5194/acp-19-245-2019), 2019.

1467 Smirnov, A., Holben, B., Slutsker, I., Giles, D., McClain, C., Eck, T., Sakerin, S., Macke, A., Croot, P.,
1468 and Zibordi, G.: Maritime aerosol network as a component of aerosol robotic network, *J. Geophys. Res-*
1469 *Atmos.*, 114, <https://doi.org/10.1029/2008JD011257>, 2009.

1470 Streets, D. G., Yan, F., Chin, M., Diehl, T., Mahowald, N., Schultz, M., Wild, M., Wu, Y., and Yu, C.:
1471 Anthropogenic and natural contributions to regional trends in aerosol optical depth, 1980–2006, *J.*
1472 *Geophys. Res-Atmos.*, 114, <https://doi.org/10.1029/2008JD011624>, 2009.

1473 Sun, E., Xu, X., Che, H., Tang, Z., Gui, K., An, L., Lu, C., and Shi, G.: Variation in MERRA-2 aerosol
1474 optical depth and absorption aerosol optical depth over China from 1980 to 2017, *J. Atmos. Sol-Terr.*
1475 *Phy.*, 186, 8-19, <https://doi.org/10.1016/j.jastp.2019.01.019>, 2019.

1476 Sun, Y. and Zhao, C.: Influence of Saharan dust on the large-scale meteorological environment for
1477 development of tropical cyclone over North Atlantic Ocean Basin, *J. Geophys. Res-Atmos.*, 125,
1478 e2020JD033454, <https://doi.org/10.1029/2020JD033454>, 2020.

1479 Teixeira, A.: Classification and regression tree, *Rev. Mal. Respir.*, 21, 1174-1176,
1480 [https://doi.org/10.1016/S0761-8425\(04\)71596-X](https://doi.org/10.1016/S0761-8425(04)71596-X), 2004.

1481 Tian, X., Tang, C., Wu, X., Yang, J., Zhao, F., and Liu, D.: The global spatial-temporal distribution and
1482 EOF analysis of AOD based on MODIS data during 2003-2021, *Atmos. Environ.*, 302,
1483 <https://doi.org/10.1016/j.atmosenv.2023.119722>, 2023.

1484 Tupper, A., Oswalt, J. S., and Rosenfeld, D.: Satellite and radar analysis of the volcanic-cumulonimbi at
1485 Mount Pinatubo, Philippines, 1991, *J. Geophys. Res-Atmos.*, 110,
1486 <https://doi.org/10.1029/2004JD005499>, 2005.

1487 van der Veer, G., Voerkelius, S., Lorentz, G., Heiss, G., and Hoogewerff, J. A.: Spatial interpolation of
1488 the deuterium and oxygen-18 composition of global precipitation using temperature as ancillary variable,
1489 *Journal of Geochemical Exploration*, 101, 175-184, <https://doi.org/10.1016/j.gexplo.2008.06.008>, 2009.

1490 Vernier, J. P., Thomason, L. W., Pommereau, J. P., Bourassa, A., Pelon, J., Garnier, A., Hauchecorne, A.,
1491 Blanot, L., Trepte, C., and Degenstein, D.: Major influence of tropical volcanic eruptions on the
1492 stratospheric aerosol layer during the last decade, *Geophys. Res. Lett.*, 38,
1493 <https://doi.org/10.1029/2011GL047563>, 2011.

1494 Wang, K., Dickinson, R. E., and Liang, S.: Clear Sky Visibility Has Decreased over Land Globally from
1495 1973 to 2007, *Science*, 323, 1468-1470, <https://doi.org/10.1126/science.1167549>, 2009.

1496 Wang, K. C., Dickinson, R. E., Su, L., and Trenberth, K. E.: Contrasting trends of mass and optical
1497 properties of aerosols over the Northern Hemisphere from 1992 to 2011, *Atmos. Chem. Phys.*, 12, 9387-
1498 9398, <https://doi.org/10.5194/acp-12-9387-2012>, 2012.

1499 Wei, J., Li, Z., Peng, Y., and Sun, L.: MODIS Collection 6.1 aerosol optical depth products over land and
1500 ocean: validation and comparison, *Atmos. Environ.*, 201, 428-440,
1501 <https://doi.org/10.1016/j.atmosenv.2018.12.004>, 2019.

1502 Wei, J., Li, Z., Sun, L., Peng, Y., Liu, L., He, L., Qin, W., and Cribb, M.: MODIS Collection 6.1 3 km
1503 resolution aerosol optical depth product: Global evaluation and uncertainty analysis, *Atmos. Environ.*,
1504 240, 117768, <https://doi.org/10.1016/j.atmosenv.2020.117768>, 2020.

1505 Welton, E. J., Campbell, J. R., Berkoff, T. A., Spinhirne, J. D., and Starr, D. O.: The micro-pulse lidar
1506 network (MPLNET), *Frontiers in Optics*, <https://doi.org/10.1364/fio.2003.mk2>, 2002.

1507 Winker, D. M., Tackett, J. L., Getzewich, B. J., Liu, Z., Vaughan, M. A., and Rogers, R. R.: The global
1508 3-D distribution of tropospheric aerosols as characterized by CALIOP, *Atmos. Chem. Phys.*, 13, 3345-
1509 3361, <https://doi.org/10.5194/acp-13-3345-2013>, 2013.

1510 Winker, D. M., Vaughan, M. A., Omar, A., Hu, Y., Powell, K. A., Liu, Z., Hunt, W. H., and Young, S. A.:
1511 Overview of the CALIPSO Mission and CALIOP Data Processing Algorithms, *J. Atmos. Ocean. Tech.*,
1512 26, 2310-2323, <https://doi.org/10.1175/2009jtecha1281.1>, 2009.

1513 Wu, J., Luo, J., Zhang, L., Xia, L., Zhao, D., and Tang, J.: Improvement of aerosol optical depth retrieval
1514 using visibility data in China during the past 50years, *J. Geophys. Res-Atmos.*, 119, 13370-13387,
1515 <https://doi.org/10.1002/2014jd021550>, 2014.

1516 Xia, X., Che, H., Zhu, J., Chen, H., Cong, Z., Deng, X., Fan, X., Fu, Y., Goloub, P., and Jiang, H.: Ground-
1517 based remote sensing of aerosol climatology in China: Aerosol optical properties, direct radiative effect
1518 and its parameterization, *Atmos. Environ.*, 124, 243-251,
1519 <https://doi.org/10.1016/j.atmosenv.2015.05.071>, 2016.

1520 Yang, X., Zhao, C., Yang, Y., and Fan, H.: Long-term multi-source data analysis about the characteristics
1521 of aerosol optical properties and types over Australia, *Atmos. Chem. Phys.*, 21, 3803-3825,
1522 <https://doi.org/10.5194/acp-21-3803-2021>, 2021a.

1523 Yang, X., Zhao, C., Yang, Y., Yan, X., and Fan, H.: Statistical aerosol properties associated with fire
1524 events from 2002 to 2019 and a case analysis in 2019 over Australia, *Atmos. Chem. Phys.*, 21, 3833-
1525 3853, <https://doi.org/10.5194/acp-21-3833-2021>, 2021b.

1526 Yang, X., Wang, Y., Zhao, C., Fan, H., Yang, Y., Chi, Y., Shen, L., and Yan, X.: Health risk and disease
1527 burden attributable to long-term global fine-mode particles, *Chemosphere*, 287,
1528 <https://doi.org/10.1016/j.chemosphere.2021.132435>, 2022.

1529 Yang, Y., Ge, B., Chen, X., Yang, W., Wang, Z., Chen, H., Xu, D., Wang, J., Tan, Q., and Wang, Z.:
1530 Impact of water vapor content on visibility: Fog-haze conversion and its implications to pollution control,
1531 *Atmos. Res.*, 256, <https://doi.org/10.1016/j.atmosres.2021.105565>, 2021c.

1532 Yoon, J., Burrows, J., Vountas, M. v., von Hoyningen-Huene, W., Chang, D., Richter, A., and Hilboll, A.:
1533 Changes in atmospheric aerosol loading retrieved from space-based measurements during the past decade,
1534 *Atmos. Chem. Phys.*, 14, 6881-6902, <https://doi.org/10.5194/acp-14-6881-2014>, 2014.

1535 Yoon, J., Pozzer, A., Chang, D. Y., Lelieveld, J., Kim, J., Kim, M., Lee, Y., Koo, J.-H., Lee, J., and Moon,
1536 K.: Trend estimates of AERONET-observed and model-simulated AOTs between 1993 and 2013, *Atmos.*
1537 *Environ.*, 125, 33-47, <https://doi.org/10.1016/j.atmosenv.2015.10.058>, 2016.

1538 Zhang, S., Wu, J., Fan, W., Yang, Q., and Zhao, D.: Review of aerosol optical depth retrieval using
1539 visibility data, *Earth-Sci. Rev.*, 200, 102986, <https://doi.org/10.1016/j.earscirev.2019.102986>, 2020.
1540 Zhang, Z., Wu, W., Wei, J., Song, Y., Yan, X., Zhu, L., and Wang, Q.: Aerosol optical depth retrieval from
1541 visibility in China during 1973-2014, *Atmos. Environ.*, 171, 38-48,
1542 <https://doi.org/10.1016/j.atmosenv.2017.09.004>, 2017.
1543 Zhao, A. D., Stevenson, D. S., and Bollasina, M. A.: The role of anthropogenic aerosols in future
1544 precipitation extremes over the Asian Monsoon Region, *Clim. Dynam.*, 52, 6257-6278,
1545 <https://doi.org/10.1007/s00382-018-4514-7>, 2019.
1546